

www.acsanm.org Article

# Investigation of Ni/Ni<sub>3</sub>C Nanoparticle Synthesis for Application as a Catalyst in Carbon Nanostructure Growth

Crystian W. C. Silva, Gabriel A. Cabrera-Pasca, Katiusse S. Souza, Cleidilane S. Costa, Messias S. Costa, Bruno S. Correa, Wanderson L. Ferreira, Rafael S. Freitas, Artur W. Carbonari,\* and Larissa Otubo\*



Cite This: ACS Appl. Nano Mater. 2023, 6, 20623-20638



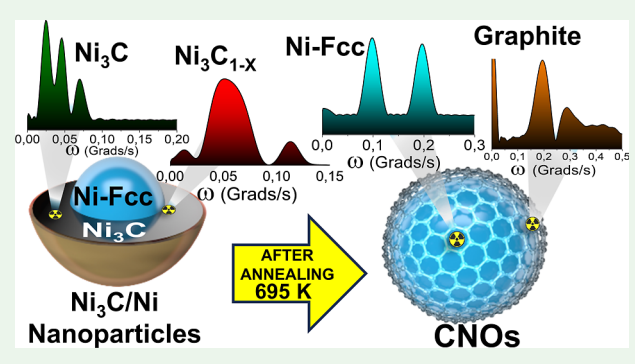
**ACCESS** I

III Metrics & More

Article Recommendations

s Supporting Information

ABSTRACT: The synthesis of functional Ni/Ni<sub>3</sub>C nanoparticles has attracted significant interest, especially in the field of electrocatalysis, where these promising nanoparticles are employed to develop sophisticated electrocatalysts, particularly for hydrogen production through the hydrogen evolution reaction. However, the significant reactivity of these systems makes them susceptible to degradation, compromising their catalyst performance. One solution explored to mitigate this problem involves the catalytic growth of carbon nanostructures to encapsulate and protect these nanoparticles. The mechanisms for the formation of carbon nanostructures from nanoparticles remain the subject of this study. Among the reported processes, the annealing of nanocatalysts has been described as a



highly effective method for producing such systems. This process is influenced by parameters, such as the temperature, atmosphere, and structural and morphological characteristics of the nanocatalysts. In the work reported here, we evaluated the influence of different ligand pairs (oleylamine/oleic acid and oleylamine/palm kernel oil) on the structural, morphological, and magnetic properties of Ni/Ni<sub>3</sub>C nanoparticles obtained through thermal decomposition at 240 °C for 3 h. Additionally, we investigated the impact of annealing in a nitrogen atmosphere on the structural properties of these nanoparticles and the growth of carbon nanostructures as a protective mechanism. The analyses include conventional techniques such as X-ray diffraction, transmission electron microscopy (TEM), magnetization measurements, and thermogravimetric analysis with differential scanning calorimetry. Additionally, local analysis was conducted using perturbed angular correlation spectroscopy (PAC) across a broad temperature range (30-693 K), utilizing the radioactive tracer <sup>111</sup>In(<sup>111</sup>Cd) for these measurements. The characterizations revealed that palm kernel oil contributes to the formation of nanoparticles with a higher Ni<sub>3</sub>C content, a broader size distribution, and a lower saturation magnetization. The PAC measurements in the range of 30-50 K, along with density functional theory calculations, indicated the absence of the Ni-hcp phase in the nanoparticles, a topic frequently discussed in the literature. Moreover, the presence of Ni<sub>3</sub>C regions with carbon deficiency was identified, characterized by a quadrupole frequency ( $\nu_{\rm Q}$ ) of 23 MHz and a hyperfine field ( $B_{\rm hf}$ ) of 1 T. The temperature-dependent local analysis, combined with thermal analysis and TEM measurements, confirmed the development of carbon nano-onions around the nanoparticles during thermal treatment above 695 K in a nitrogen atmosphere. This observation demonstrates that nanoparticles obtained with palm kernel oil, which has the highest Ni<sub>3</sub>C content, offer superior encapsulation of Ni nuclei through these graphitic nanostructures.

**KEYWORDS:** ligands, nanoparticles, catalytic, graphitization, hyperfine interactions

# 1. INTRODUCTION

The synthesis of transition metal nanoparticles encapsulated by transition-metal carbides has been the focus of recent research. This is particularly significant because crystallization of these materials combines the intrinsic properties of transition metals such as high magnetic moments, superparamagnetism, and excellent catalytic activity with the chemical stability and high thermal and electrical conductivity of metallic carbides such as Fe<sub>3</sub>C, Co<sub>2</sub>C, Co<sub>3</sub>C, and Ni<sub>3</sub>C. These enhanced nanoparticles are appealing for a wide range of applications, especially in the development of sophisticated catalysts for the hydrogen evolution reaction (HER).  $^{3,8}$ 

However, a limiting factor for this application is the formation of strong bonds between  $H_2$  and transition metals during the process, which lead to the degradation of these catalysts and compromise their catalytic performance.<sup>10,11</sup>

Received: July 12, 2023
Revised: October 24, 2023
Accepted: October 25, 2023
Published: November 8, 2023





Scheme 1. Schematic Representation of the Synthesis of Ni<sub>3</sub>C Nanoparticles with a Ni-fcc Core with Radioactive <sup>111</sup>In



An interesting alternative that has been explored in recent research for obtaining functional nanocatalysts for HERs is the encapsulation of transition metal nanoparticles in carbon nanostructures, such as graphene, <sup>12</sup> carbon nanotubes, <sup>13,14</sup> and carbon nano-onions (CNOs). <sup>15</sup> In this process, the formation of a graphitic structure or shell provides chemical stability and contributes to the catalytic efficiency of the nanoparticles. Among the main catalytic growth processes for these nanostructures, chemical vapor deposition, arc discharge, pyrolysis, and annealing are reported in the literature.<sup>19</sup> The annealing process of precursor nanoparticles in a controlled atmosphere has been described as a high-yield method applicable on an industrial scale, making it particularly appealing. However, the mechanisms governing the growth of graphitic nanostructures from nanoparticles are still under investigation.<sup>21</sup> Previous reports demonstrate that the growth of these nanostructures depends on parameters such as the temperature and synthesis atmosphere, as well as the size, morphology, and carbon content of the precursor nano-particles. Thus, transition-metal nanoparticles encapsulated by transition-metal carbides such as Fe/FeC, Co/Co<sub>2</sub>C, and Ni/Ni<sub>3</sub>C, with a well-established structure and morphology, can facilitate the systematic growth of graphitic nanostructures. 8,24-26 Among these hierarchical systems, Nibased nanoparticles have gained significant attention from the scientific community in recent years due to their exceptional catalytic and magnetic properties. 16 Consequently, a series of studies have investigated the catalytic performance of Ni nanostructures, including nitrides, 27 phosphides, 28 oxides, 29 hydroxides,<sup>30</sup> and carbides.<sup>31</sup>

Despite all these Ni nanoparticle systems holding catalytic significance, Ni/Ni $_3$ C nanoparticles have garnered particular interest due to their ease of synthesis through chemical routes and their promising role as catalysts in the self-assembly and growth of carbonaceous nanomaterials, <sup>14</sup> particularly CNOs. <sup>32,33</sup> These carbon nanostructures consist of hierarchically stacked fullerene-like structures, resembling the layers of an onion, with thicknesses ranging from 2 to 100 nm, and they exhibit high electrical conductivity. <sup>24,34,35</sup> The hierarchical structure of Ni/Ni $_3$ C nanoparticles enables the encapsulation of Ni nanoparticles within CNOs through the catalytic graphitization of amorphous carbon during annealing at

temperatures above 300 °C under an inert atmosphere, as demonstrated in the literature. <sup>36,37</sup> This process enhances the resistance of nanoparticles to corrosive chemical and physical environments, extending the lifespan of catalysts based on these materials and further improving their optical and photocatalytic properties. <sup>11,32</sup> However, the growth of carbon nanostructures in Ni/Ni<sub>3</sub>C systems is dependent on parameters such as the size, morphology, atmosphere, proportion of crystalline phases, and surface functionalization of these nanoparticles, which can be controlled through parametrized synthesis processes. As a result, a number of synthesis protocols have been developed with the goal of controlling the shape, size, and functionality of the surfaces of these materials. <sup>11,21</sup>

Among these synthesis methods, "bottom-up" processes such as polyol,  $^{38}$  sonochemistry,  $^{39}$  and thermal decomposition  $^{40-42}$  should be highlighted. These methods are based on the controlled decomposition of metallic salts in the presence of ligands, whose function is to promote precursor reduction and stabilize nanoparticle formation during the growth stage. The use of the oleylamine/oleic acid ligand pair in obtaining Ni/Ni<sub>3</sub>C-type nanoparticles by chemical routes has been frequently reported due to its effectiveness and affordability. Because they are hard Lewis bases, these ligands form complexes with the precursor metallic ions under controlled conditions that can be thermally decomposed, promoting nanoparticle nucleation and growth. As a result, the interaction between oleic acid and oleylamine influences the shape, size, crystalline structure, and capping of these nanoparticles.

The influence of these synthesis protocols on the structural properties of these nanoparticles is being investigated, specifically because the crystallization of Ni-hcp or Ni<sub>3</sub>C phases during synthesis in the presence of oleic acid and oleylamine is not yet well established, primarily due to the structural and magnetic similarities between these structures. The rhombohedral structure (space group:  $R\ \bar{3}\ c$ ) of Ni<sub>3</sub>C is defined as a Ni-hcp structure with an interstitial carbon superstructure. In this regard, the X-ray diffraction (XRD) patterns of Ni<sub>3</sub>C and Ni-hcp are difficult to distinguish. Moreover, the lattice parameters assigned to Ni-hcp in some experimental reports (a=0.2648-0.2660 nm and c=0.4328-

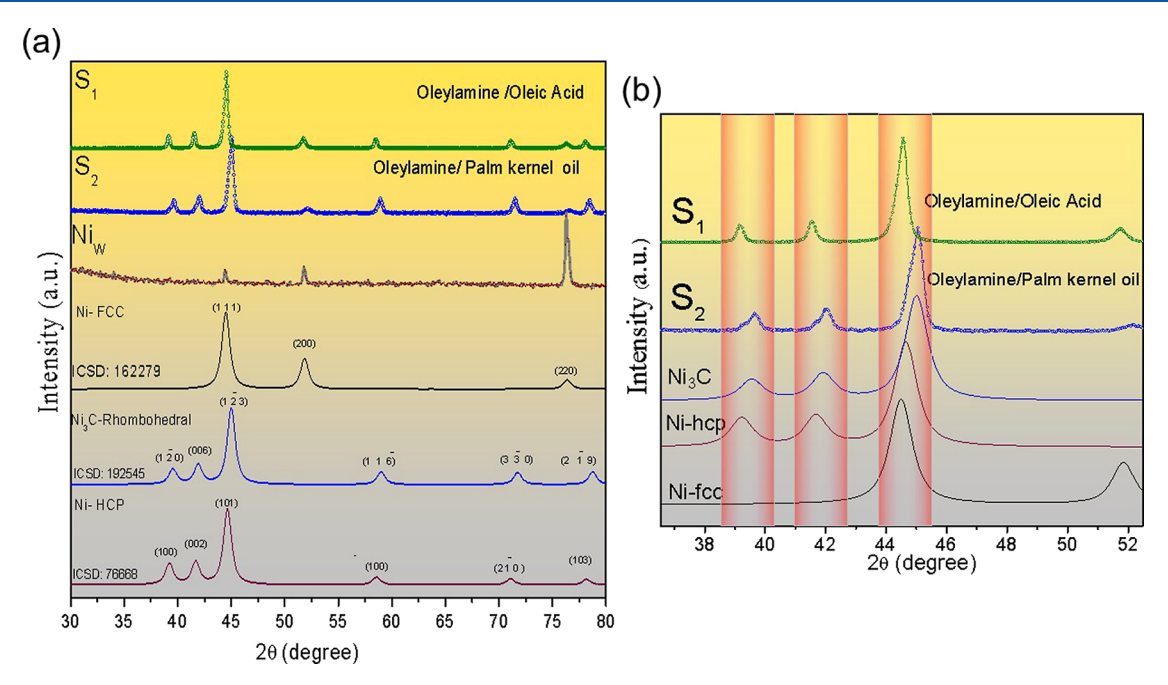


Figure 1. (a) Experimental  $(S_1, S_2, and Ni_w)$  and theoretical XRD patterns for Ni-fcc, Ni<sub>3</sub>C, and Ni-hcp. (b) Comparison between the theoretical and experimental XRD patterns, showing a shift toward larger angles in  $S_2$ , which suggests the formation of a higher concentration of Ni<sub>3</sub>C relative to  $S_1$ .

0.4339 nm) show greater similarity to Ni<sub>3</sub>C (a = 0.2628 nm and c = 0.4306 nm) than to the theoretically predicted parameters for Ni-hcp (a = 0.2500 nm and c = 0.3980 nm).  $^{42,45,46}$ 

The magnetic properties of these phases further complicate the distinction between them. Due to the strong hybridization between Ni and C orbitals, diamagnetic behavior is predicted for Ni<sub>3</sub>C, while ferromagnetic behavior is predicted for Ni-hcp. Thowever, the reported magnetic properties of Ni-hcp nanoparticles in some experimental reports vary from non-magnetic to weakly magnetic. These findings can be attributed to both Ni<sub>3</sub>C and carbon-deficient Ni<sub>3</sub>C. Disagreements in the literature regarding the metastable nature of Ni-hcp and the ease with which Ni can be contaminated by C, N, B, and H atoms suggest that Ni<sub>3</sub>C was possibly misidentified as Ni-hcp in earlier reports. <sup>36,39,49</sup>

The necessity for well-established crystalline properties to optimize the application of these systems has prompted numerous studies to investigate the mechanisms of formation and decomposition of these phases. Xing et al., for example, reported the influence of the carbon content on small shifts to higher angles in XRD patterns obtained under statistical conditions for Ni<sub>3</sub>C nanoparticles. The findings reported by Chiang et al. demonstrate that annealing Ni<sub>3</sub>C nanoparticles at 500 °C can produce a Ni-hcp structure free of interstitial atoms, indicating that this specific structure can be obtained during the transition from Ni<sub>3</sub>C to Ni-fcc. These published studies highlight the challenges of identifying these crystalline formations (Scheme 1).

The mechanism of Ni<sub>3</sub>C formation was also explored by the reduction of Ni salts through thermolysis in the presence of oleylamine and oleic acid. Because of differences in binding mode strengths and reduction abilities, ligands play a key role in this route. <sup>43</sup> Often, oleylamine acts as a reducing agent, while oleic acid mainly controls the size and holds the particles together. <sup>51</sup> After the reduction of the precursor, the ligands are

adsorbed on the surface of the Ni monomers; these molecules decompose into active carbon by the catalytic action of Ni, and under suitable conditions these carbon atoms diffuse into the Ni lattice, promoting the formation of Ni<sub>3</sub>C regions. Due to its higher decomposition temperature, oleic acid acts as a surfactant that regulates the growth of these nanoparticles, resulting in nanoparticles coated with an organic layer. As, S3

The coating or encapsulation of nanoparticles is critical to their stability and functionality. The increasing possibility of producing functional nanoparticles with biocompatible properties has driven up the usage of various ligands as scaffolding for nanoparticles, particularly ligands of plant origin. 4,54,55 Correa et al. used Açai (Euterpe oleracea Mart.), Ucuúba (Virola surinamensis), and Bacaba (Oenocarpus bacaba Mart.) oils, extracted by supercritical CO2, as a green alternative in the thermal decomposition method to synthesize Fe<sub>3</sub>O<sub>4</sub> nanoparticles, resulting in enhanced superparamagnetic behavior with higher saturation magnetization values.<sup>5</sup> As a result, there is clear evidence that using natural oils as ligands in the synthesis and coating of nanoparticles can result in morphological and structural characteristics critical to magnetic properties and biocompatibility of nanoparticles. 56,5 Furthermore, the presence of an organic coating on Ni/Ni<sub>3</sub>C nanoparticles may contribute to their application in carbon nanostructure growth, as has been observed in the literature for coated and supported nanoparticles in organic materials.<sup>58,59</sup>

A significant technological and cost-effective alternative to produce Ni/Ni<sub>3</sub>C nanoparticles among the "natural oils" is the use of palm kernel oil, which is obtained from the seed of palm fruit (*Elaeis guineensis*). Palm kernel oil not only has great commercial applicability as a raw material for the food, chemical, and cosmetic industries but also is composed of saturated and unsaturated fatty acids with long carbon chains (for example, lauric acid, palmitic acid, oleic acid, and myristic acid) that are perfect for coating and surface-functionalizing nanoparticles. <sup>60,61</sup> Moreover, the successful synthesis of iron-

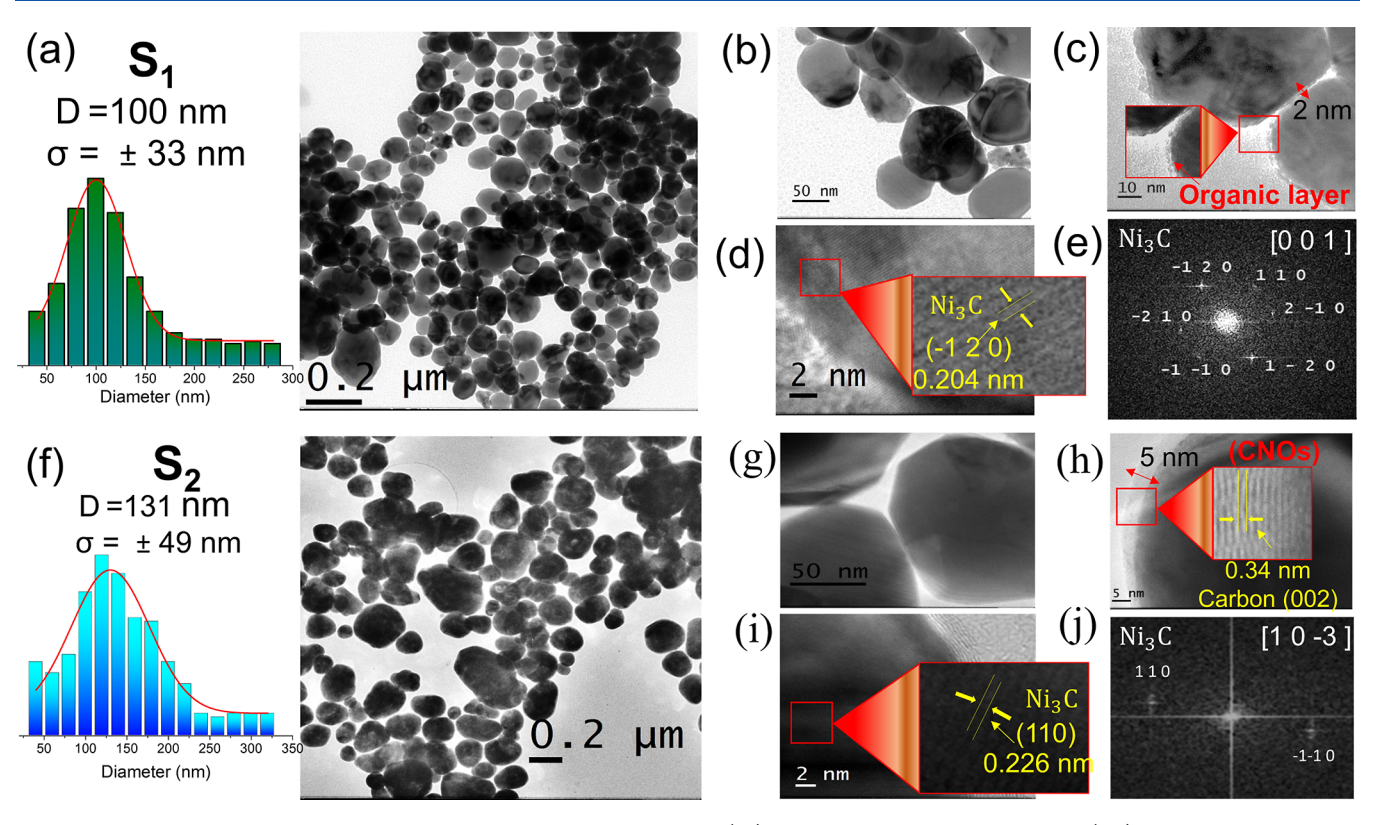


Figure 2. Structure and morphology of samples  $S_1$  and  $S_2$  observed by TEM. (a,f) Morphology and size distribution. (b,g) Micrographs at a higher magnification. (c,h) Organic material adsorbed on the surface of the nanoparticles. (d,i) HRTEM micrographs of  $S_1$  and  $S_2$ , respectively. (e,j) FFTs for  $S_1$  and  $S_2$ , respectively. Only the planes referring to Ni<sub>3</sub>C are shown according to the indexation of the planes in the aforementioned zonal axes.

doped  $\text{Co}_3\text{O}_4$  nanoparticles using palm kernel oil has been reported in the literature.  $^{62}$ 

In this report, we investigate whether the use of different pairs of ligands has an impact on the morphological and structural characteristics of Ni/Ni<sub>3</sub>C nanoparticles and whether it is possible to examine the local effects of the ligand pair on the structural and magnetic properties at the atomic scale. By using the ligand pairs oleylamine/oleic acid and oleylamine/palm kernel oil, we present a comprehensive and comparative analyses of the production and characterization of Ni/Ni<sub>3</sub>C core/shell nanoparticles. Additionally, we investigated the decomposition mechanism of these systems through annealing in a nitrogen atmosphere and its influence on the growth of carbon nanostructures.

The synthesized nanoparticles were characterized by using X-ray diffractometry (XRD), transmission electron microscopy (TEM), high-resolution transmission electron microscopy (HRTEM), magnetization measurements, and thermogravimetric analysis/differential scanning calorimetry (TGA/DSC). The primary method used for analyzing the crystalline phases locally was perturbed angular correlation spectroscopy (PAC), which covered a wide temperature range (30-700 K). As a nonresonant nuclear technique, PAC spectroscopy enables local atomic study as well as the observation of structural and magnetic changes at high-temperature ranges. 63,64 The local properties obtained using PAC were correlated with those obtained by using conventional characterization techniques. In addition, ab initio calculations were performed using the computational package WIEN2k, using the LAPW method (linearized augmented plane wave) and the GGA approximation (generalized gradient approximation) within the Kohn-Sham scheme for density functional theory (DFT)

calculations, which provided validation for the experimentally obtained hyperfine parameters.

# 2. RESULTS AND DISCUSSION

Figure 1 displays the XRD results, providing information on the structural characteristics of samples. The diffractogram shown for the Ni<sub>w</sub> sample is compatible with that for Ni-fcc, as predicted for elemental Ni (ICSD-162279), indicating a preferential orientation along the plane (220), which can be attributed to the geometric characteristic of the sample.<sup>65</sup> For both synthesized nanoparticle samples  $(S_1 \text{ and } S_2)$ , the diffraction patterns can be attributed to the rhombohedral Ni<sub>3</sub>C (ICSD-192545) and Ni-fcc (ICSD-162279) structures, suggesting mixed Ni/Ni<sub>3</sub>C nanoparticles. The proportion of the phases obtained according to the Rietveld refinement indicates that the S<sub>1</sub> sample has 30% Ni-fcc and 70% Ni3C, while the S<sub>2</sub> sample has 12% Ni-fcc and 88% Ni3C (see Figure S1 in the Supporting Information), suggesting, therefore, that the use of palm kernel oil as a solvent and surfactant favors the formation of nanoparticles (S<sub>2</sub>) with a higher Ni<sub>3</sub>C content when compared to nanoparticles synthesized with oleic acid  $(S_1)$ .

These results are illustrated in Figure 1b, where it is possible to notice that nanoparticles obtained using oleic acid  $(S_1)$  show a diffraction pattern with greater similarity to the Ni-hcp structure, probably due to the lower interstitial carbon content. On the other hand, the diffraction peaks of nanoparticles synthesized using palm kernel oil  $(S_2)$  show a shift to larger angles, which may be indicative of a higher interstitial carbon content, as shown by Xing et al. <sup>50</sup> The average crystallite size was determined according to the Scherrer equation as 15 and 19 nm for  $S_1$  and  $S_2$ , respectively.

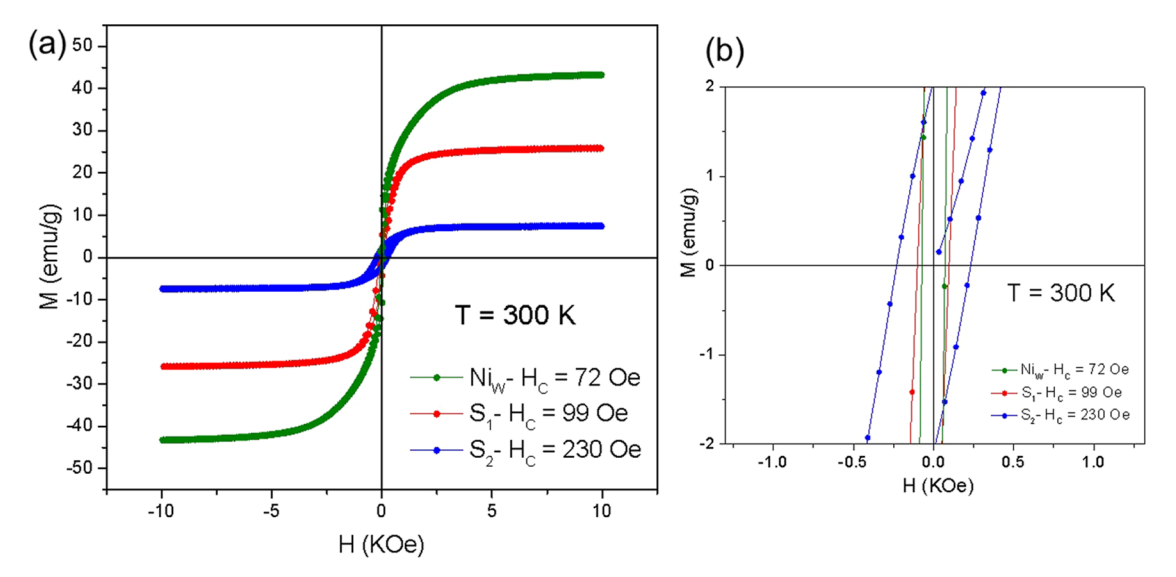


Figure 3. Magnetization by the applied field (H) at 300 K for Ni<sub>w</sub>, S<sub>1</sub>, and S<sub>2</sub>. (a) Magnetization curves for the three samples. (b) Magnification of the magnetization around H = 0 for observing the behavior of the magnetic coercivity.

Representative TEM images of  $S_1$  and  $S_2$  samples (Figure 2a,f) show spherical nanoparticles with Gaussian size distribution and mean diameters of 100 nm with standard deviation  $\sigma = \pm$  33 nm for  $S_1$  and 131 nm with standard deviation  $\sigma = \pm$  49 nm for  $S_2$ , indicating the influence of palm kernel oil as a surfactant on the nanoparticle size.

Surfactants have the property of preventing agglomeration and stabilizing the particle size during nanoparticle formation. Palm kernel oil contains a higher amount of saturated acids [45.55% lauric acid (C12:0), 16.43% myristic acid (C14:0), and 9.53% palmitic acid (C16:0)] compared to unsaturated fatty acids [17.77% oleic acid (C18:1)]. The size and structure of nanoparticles have been reported to be effectively controlled by the use of saturated fatty acids, particularly lauric acid (which is found in a higher percentage in palm kernel oil), which has been observed for Fe<sub>3</sub>O<sub>4</sub> nanoparticles in the literature. <sup>5</sup>

The diversity of fatty acids in palm kernel oil facilitated the formation of different ligand pairs during the nucleation and growth stages of sample S2, compared to the oleylamine/oleic acid ligand pair used in sample S<sub>1</sub>. During the nucleation stage, these different ligand pairs (oleylamine/lauric acid, oleylamine/myristic acid, and oleylamine/myristic acid) bound to the surface of Ni nuclei in the form of carboxylates, promoting a heterogeneous nucleation process.<sup>67</sup> Because of the gradient in carbon concentration and the catalytic activity of the Ni nuclei, these ligands gradually diffused onto the surface of the Ni nuclei during the growth stage.  $^{41-43}$  Although samples  $S_1$ and S<sub>2</sub> go through a similar formation process, palm kernel oil induced greater growth of active carbon, which promoted the formation of regions with a higher content of Ni<sub>3</sub>C, as observed by XRD. This is because saturated fatty acids have a higher proportion of varied chain lengths in palm kernel oil. In addition, compared with S<sub>1</sub>, nanoparticles have a broader size distribution.

Figure 2b-d and g-i shows TEM images of samples  $S_1$  and  $S_2$  at higher magnifications. Figure 2c shows that nanoparticles in sample  $S_1$  are coated with an organic layer ( $\sim$ 2 nm). These results indicate that during synthesis, the prior formation of  $Ni_3C$  shells acted as a barrier, preventing contact between carbon from outer regions and the catalytic Ni nuclei, leading

to the creation of Ni/Ni<sub>3</sub>C nanoparticles coated with the organic material. For nanoparticles in sample  $S_2$ , the formation of a surface layer of organic material was also observed. The presence of organic material on the nanoparticle surface was confirmed by FTIR measurements, as shown in Figure S4 Supporting Information. After exposing sample S<sub>2</sub> to an electron beam (Figure 2h), the formation of a crystalline layer (~5 nm) with an interplanar distance of 0.34 nm was observed, consistent with the graphite (002) plane. This behavior suggests a higher propensity for the catalytic graphitization of these nanoparticles, leading to the formation of CNOs. 17,21 This process occurs due to the decomposition of carbon-supersaturated Ni<sub>3</sub>C regions, where carbon segregates and crystallizes as graphite carbon on the nanoparticle surface due to the greater thermodynamic stability of graphite carbon compared to Ni<sub>3</sub>C.<sup>37</sup>

The presence of  $Ni_3C$  in the surface of the nanoparticles can be observed in Figure 2 through fast Fourier transforms (FFTs) shown in Figure 2e,j, corresponding to the high-resolution micrographs of Figure 2d,i for  $S_1$  and  $S_2$ , respectively. The obtained and indexed patterns show only crystalline planes corresponding to  $Ni_3C$ . This observation, in addition to the XRD results, suggests the formation of nanoparticles with a Ni-fcc core and a  $Ni_3C$  shell covered with the organic material adsorbed on their surface.

The magnetic character of the samples was investigated by magnetization measurements, and the M(H) dependence of the samples was recorded at 300 K for the Ni<sub>w</sub>, S<sub>1</sub>, and S<sub>2</sub> samples. Figure 3a shows that the Ni<sub>w</sub> sample presents the highest saturation magnetization (43.25 emu/g) attributed to the Ni-fcc structure. For S<sub>1</sub> and S<sub>2</sub> nanoparticles, the saturation magnetization values were 25.80 and 7.40 emu/g, respectively. The significantly lower saturation magnetization for S<sub>2</sub> relative to S<sub>1</sub> may be associated with the higher Ni<sub>3</sub>C content in this sample. Al,48,50 When the behavior of magnetization curves is evaluated, this characteristic becomes more important. While the magnetization curve for Ni<sub>w</sub> is typical of ferromagnetic materials, the curves for S<sub>1</sub> and S<sub>2</sub> show a strong paramagnetic contribution due to the presence of the Ni<sub>3</sub>C phase. The magnetization curves are enlarged in Figure 3b at crossing M =

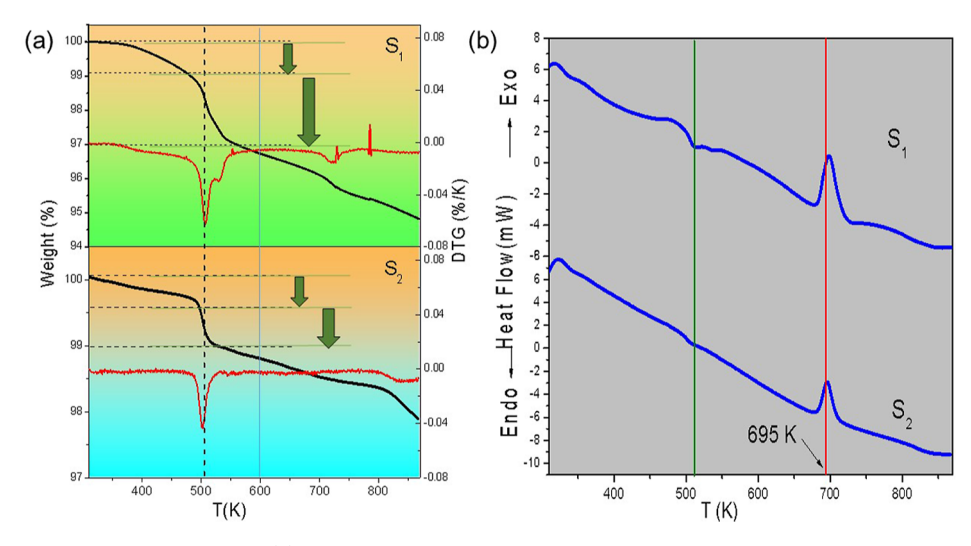


Figure 4. Thermal analysis results for  $S_1$  and  $S_2$ . (a) TGA/DTG graphs showing the decompositions that occurred in the samples in the range of 300–870 K. (b) DSC results showing an endothermic peak around 500 K related to the decomposition of surfactants on the surface of the nanoparticles, in addition to an exothermic peak at 695 K associated with a phase transition from Ni<sub>3</sub>C to Ni-fcc.

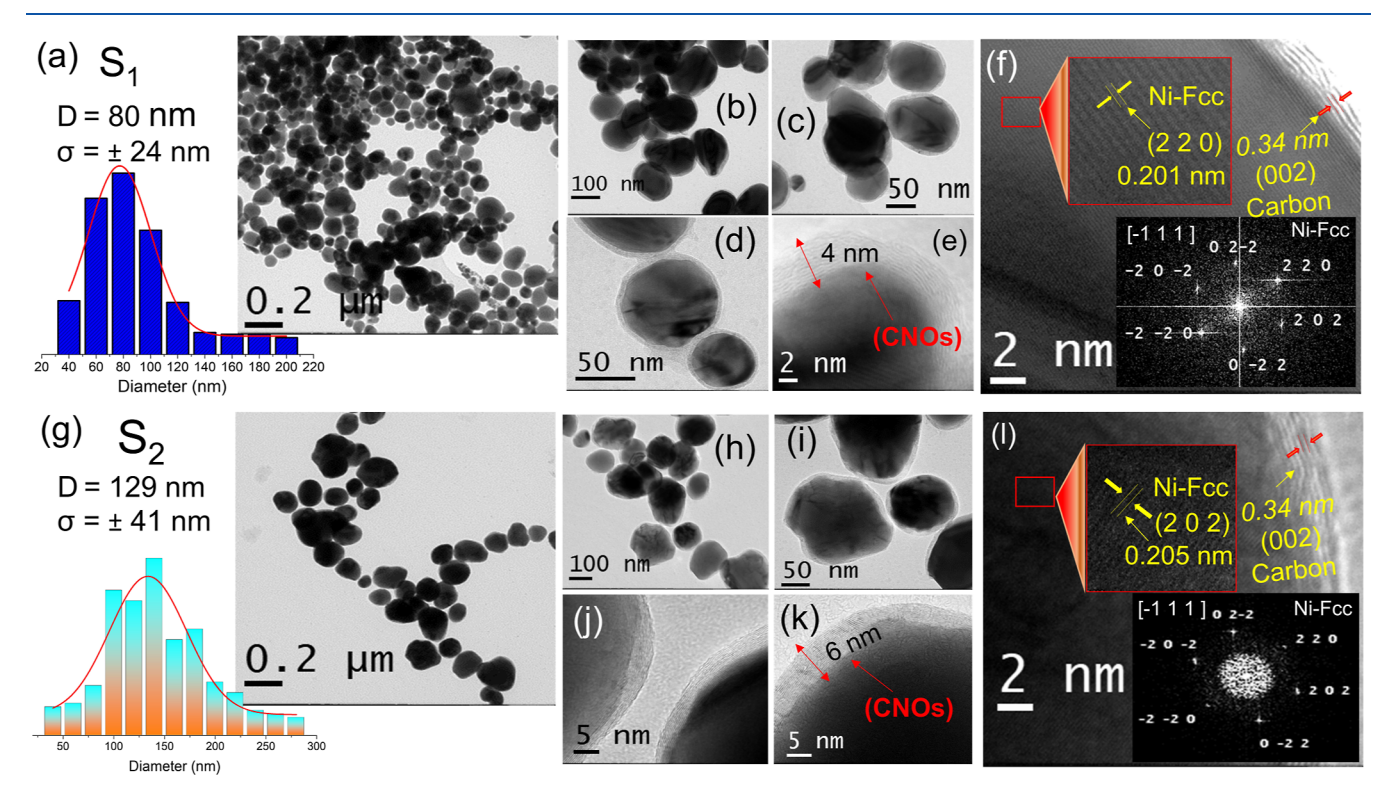


Figure 5. Structure and morphology of  $S_1$  and  $S_2$  samples after annealing. (a,g) Morphology and size distribution for  $S_1$  and  $S_2$ . (b-d) and (h-j) Micrographs with a higher magnification showing the formation of CNOs in both samples. (e,k) Morphology of the samples indicating the thickness of the graphene layers (002) of  $\sim$ 4 and  $\sim$ 6 nm for  $S_1$  and  $S_2$ , respectively. (f,l) Central regions of  $S_1$  and  $S_2$ , respectively, and the associated FFTs, which indicate the formation of Ni-fcc planes evident on the zonal axis [-1 1 1].

0, demonstrating an increase in the magnetic coercivity as the Ni<sub>3</sub>C concentration increases.

The thermal analysis results obtained for the  $S_1$  and  $S_2$  samples are shown in Figure 4. TGA and DSC curves are shown in Figure 4a,b, respectively. TGA results reveal initial weight losses for both samples at temperatures around 400 K, which may be attributed, for instance, to the evaporation of volatile substances adsorbed during washing processes. Then, as indicated by the TGA data, a mass loss between 493 and 553 K was observed, with a maximum value of roughly 500 K.

This loss can be attributed to the decomposition of the fatty acid secondary layers that were physically adsorbed on the surfaces of the nanoparticles.  $^{43,51}$  It is crucial to emphasize that  $S_1$  has a larger percentage of mass loss (around 2%). Due to its higher Ni<sub>3</sub>C content, the lower loss observed for  $S_2$  ( $\sim$ 1%) can be ascribed to the rapid crystallization of the amorphous carbon layers surrounding the particle, providing greater stability to the nanoparticles. The DSC curves presented in Figure 4b show an exothermic peak around 695 K for both nanoparticles; this behavior indicates the occurrence of a phase

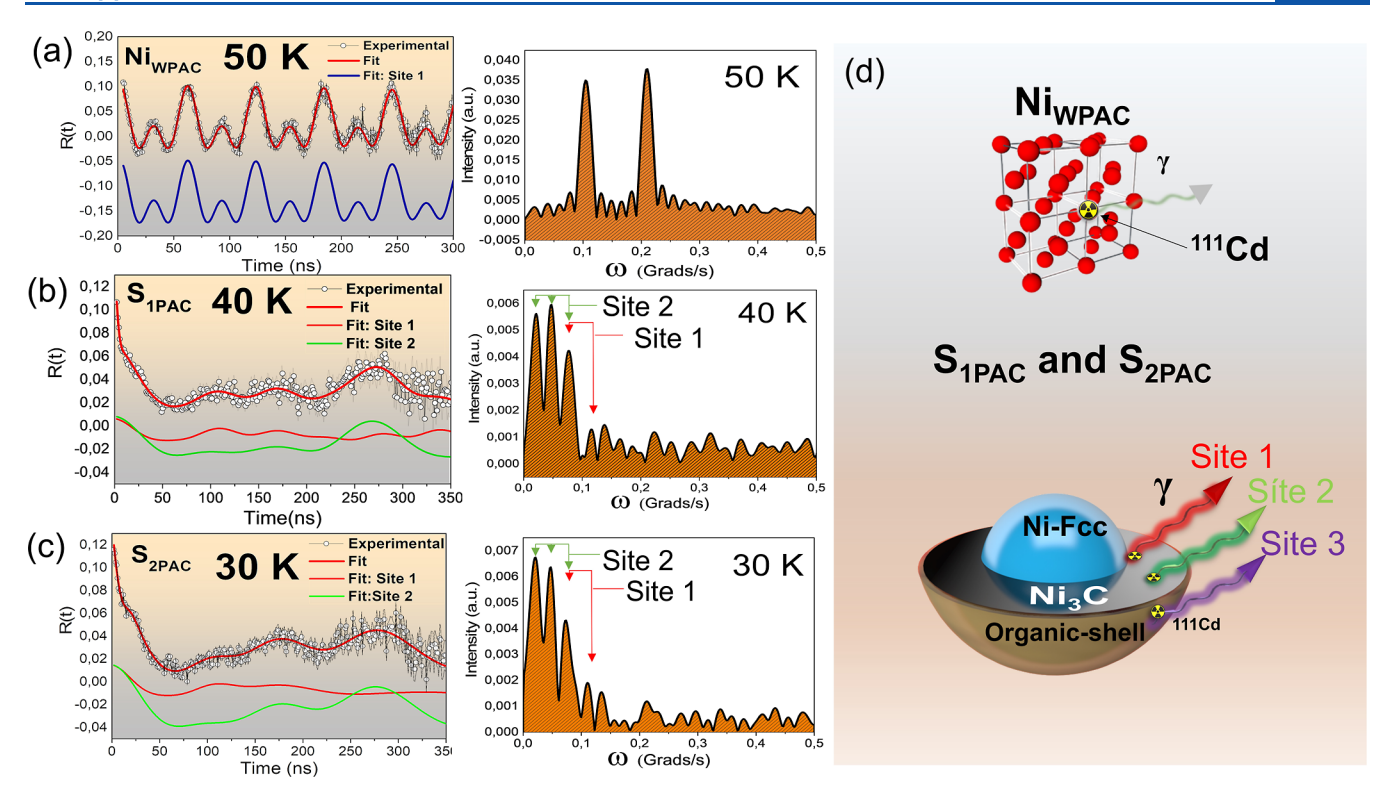


Figure 6. Anisotropy ratio functions R(t) and corresponding frequency spectra (FFT) measured using the  $^{111}In(^{111}Cd)$  probe nucleus for (a)  $Ni_{WPAC}$  in an environment with fcc symmetry. (b)  $S_{1PAC}$  and (c)  $S_{2PAC}$ . (d) Schematic representation of the location of the probe nuclei inside the nanoparticles.

transformation also observed in the decomposition of Ni<sub>3</sub>C nanoparticles into Ni and carbon, as previously reported.<sup>36</sup>

After thermal analysis,  $S_1$  and  $S_2$  samples were characterized by XRD and TEM/HRTEM to investigate the structural and morphological changes following the thermal treatment at 870 K. The XRD patterns after annealing (see Figure S5 in the Supporting Information) exhibit diffraction peaks solely corresponding to (111), (200), and (220) planes of Ni-fcc. These results are consistent with those obtained from a highpurity  $N_{I_w}$  sample, indicating that, at 695 K, a phase transition occurred for both  $S_1$  and  $S_2$ , leading to the formation of a Ni-fcc structure. The average crystallite sizes, calculated using the Scherrer equation were determined to be 26 and 29 nm for  $S_1$  and  $S_2$ , respectively.

Figure 5 shows the TEM/HRTEM images obtained after annealing at 870 K. The images presented in Figure 5a,g depict spherical nanoparticles with Gaussian size distribution and average diameters of 80 nm with standard deviation  $\sigma$  =  $\pm$  24 nm for  $S_1$  and 129 nm with standard deviation  $\sigma = \pm 41$  nm for S<sub>2</sub>. This suggests a small influence of the thermal annealing on the size distribution and morphology of the nanoparticles, indicating greater stability for the S2 sample after heat treatment. Figure 5f,l show the FFT patterns obtained for samples S<sub>1</sub> and S<sub>2</sub> after annealing. The results confirm the presence of Ni-fcc in the [-111] zone axis,<sup>68</sup> which is in agreement with the XRD results. This indicates that the original Ni<sub>3</sub>C present in the nanoparticles was transformed into Ni-fcc, facilitating the formation of Ni nanoparticles encapsulated by CNOs s, with thicknesses of 4 nm for S<sub>1</sub> and 6 nm for S<sub>2</sub> (Figure 5c-e,i-k). The annealing of catalytic nanoparticles in a controlled atmosphere has been reported as one of the main mechanisms for encapsulating nanoparticles in CNOs. 15,22,23 As observed, the formation of these structures is

dependent on the carbon concentration in the nanoparticles; the higher carbon content in sample S2 resulted in thicker CNOs (see Figure S8 in the Supporting Information). 19,21,24,26

The stability and catalytic performance of these nanoparticles are greatly influenced by the thickness of the graphene layers. As an illustration, the electrical conductivity of these structures enables the active centers to capture photogenerated electrons in applications such as cocatalysts for the photocatalytic HER. Additionally, CNOs prevent hydrogen from adhering to the surface of metal cores, preserving the catalytic efficiency. Furthermore, it has been reported in the literature <sup>17,69</sup> that the adsorption of nitrogen onto these layers through high-temperature annealing (600–900 °C) has been shown to be effective for bifunctional catalytic activity in both HER and oxygen evolution reaction (OER).

2.1. Results of Hyperfine Interactions at 111 In(111 Cd) for Radioactive Samples. The radioactive samples were characterized by perturbed angular correlation (PAC) over a wide temperature range (30 to 700 K) to carry out a local analysis through the measurements of hyperfine interactions. Figure 6 shows the anisotropy ratio functions R(t)'s and the associated FFTs, obtained at the temperatures 50, 40, and 30 K for Ni<sub>WPAC</sub>, S<sub>1PAC</sub>, and S<sub>2PAC</sub> samples, respectively. In Figure 6a, the R(t) spectrum for the Ni<sub>WPAC</sub> sample at 50 K was fitted considering a model in which  $^{111}$ In( $^{111}$ Cd) probe nuclei occupy substitutional sites in the Ni-fcc lattice and therefore considered exclusively pure magnetic hyperfine interactions, characterized by a well-defined magnetic frequency  $\mu_{\rm M} = 16$ MHz, corresponding to a hyperfine magnetic field  $B_{\rm hf}$  = 7.1 T, which is in good agreement with those found in the literature, 70-72 indicating that at a temperature of 893 K for 12 h, the 111 In(111 Cd) probes diffuse substitutionally into the crystalline Ni environment.

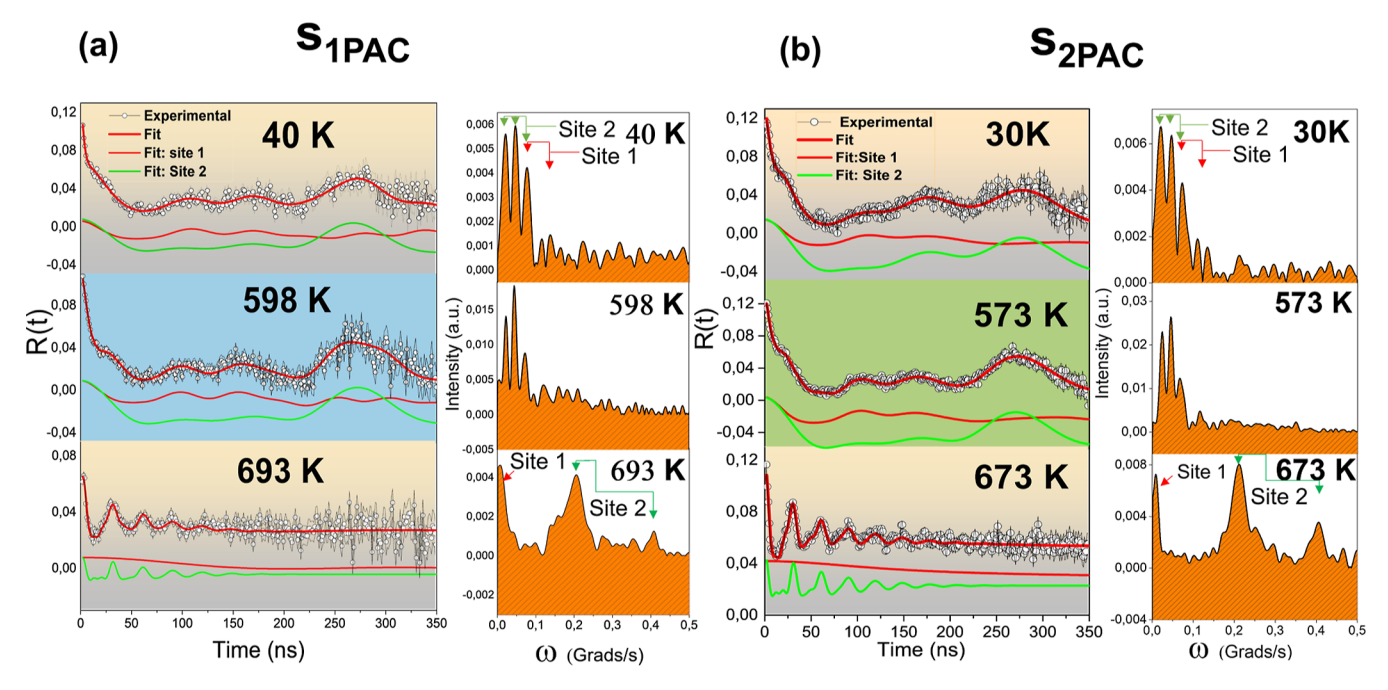


Figure 7. Anisotropy ratio functions R(t) and their FFTs in the range from 30 to 693 K showing the similarity of the functions of both  $S_1$  and  $S_2$  samples over this temperature range. (a) Representative spectra of the sample obtained with oleic acid  $(S_{1PAC})$ . (b) Representative spectra of the sample obtained using palm kernel oil  $(S_{2PAC})$ . From 600 K onward, a change in the modulation of the R(t) spectra is evident for both samples, which indicates a phase transition at this temperature.

Figure 6b,c shows the anisotropy ratio functions and the corresponding FFTs for S<sub>1PAC</sub> and S<sub>2PAC</sub> samples measured at 40 and 30 K, respectively. The R(t) functions show very similar behaviors along the time evolution (0-350 ns). For the fitting of these spectra and consequent extraction of the hyperfine parameters, a model in which the probe nuclei can occupy three site fractions was considered, named site 1, site 2, and site 3. Because of the wide distribution of the quadrupole frequency ( $\delta_3 = 0.70$ ) of site 3, only the hyperfine parameters referring to sites 1 and 2 are relevant for the discussion. Site 3 represents low-symmetry areas that are likely related to the probe nuclei adsorbed to the organic coating of the nanoparticles. Sites 1 and 2 present distributions of  $\delta_1$  = 0.01 and  $\delta_2 = 0.07$ , respectively, which justify the position of the probe in a periodic site of the crystalline lattice. Therefore, for the S<sub>1PAC</sub> sample, site 1 was fitted with a quadrupole frequency of  $\nu_0 1$  = 29 MHz and a magnetic frequency of  $\nu_M 1$ = 2.25 MHz corresponding to a hyperfine magnetic field of  $B_{\rm hf}$ = 1 T, with a null asymmetry parameter ( $\eta$  = 0). For site 2, only a quadrupole frequency of  $\nu_{\rm Q}2$  = 24 MHz was obtained, with an asymmetry parameter  $\eta = 0.20$ . The contributions of these sites in the  $R(\bar{t})$  spectrum of the  $S_{1PAC}$  sample were 20% for site 1 and 43% for site 2.

For the R(t) function referring to the  $S_{\rm 2PAC}$  sample measured at a temperature of 30 K, a quadrupole frequency  $\nu_{\rm Q1}=26$  MHz, a magnetic frequency  $\nu_{\rm M1}=2.4$  MHz ( $B_{\rm hf}$  1T) and, an asymmetry parameter  $\eta=0$  came out from the fit for site 1. For site 2, a quadrupole frequency  $\nu_{\rm Q2}=23$  MHz with an asymmetry parameter  $\eta=0.40$  was obtained. The fractions of these sites obtained for the experimental spectrum were 19 and 33%, for site 1 and site 2, respectively.

Comparing the R(t) functions and their FFTs shown in Figure 7a-c, the discrepancy in the behavior of the spectra obtained for the nanoparticles and the modulation obtained for <sup>111</sup>In(<sup>111</sup>Cd) in a Ni-fcc environment are notable. This aspect

indicates that there are no probe nuclei at substitutional sites in the Ni-fcc lattice for the nanoparticle samples. Additionally, the hyperfine parameters measured for site 1 are not compatible with those of \$^{111}In(^{111}Cd)\$ located at interstitial Ni sites, as predicted in the literature. This effectively eliminates the possibility of such occupation for the observed sites. The with what was observed for nonradioactive nanoparticles through XRD analysis. Another intriguing aspect of the local analysis is that despite the XRD and magnetization results obtained for nonradioactive samples show a higher Ni<sub>3</sub>C content for samples obtained with palm kernel oil (S<sub>2</sub>), the fractions obtained from PAC reveal the least diffusion of \$^{111}In(^{111}Cd)\$ in these nanoparticles.

This aspect is associated with the mobility of the probe through diffusion during the nanoparticle formation process. In accordance with the models already established in the literature for the formation of Ni/Ni<sub>3</sub>C nanoparticles, during the nucleation stage, the decomposition of the metallic precursor (Ni(acac)<sub>2</sub>) induces the creation of Ni nuclei, which adsorb ligand molecules associated with  $^{111}\text{In}(^{111}\text{Cd})$ . This specific association arises due to  $^{111}\text{In}(^{111}\text{Cd})$  being a strong acid and readily binding to strong bases, such as carboxylic acids and amines (oleic acid, oleylamine, and fatty acids from palm kernel oil) during the nucleation process.  $^{73,74}$ 

During the growth stage, the catalytic action of Ni is responsible for the disintegration of the molecules adsorbed on the active carbon surface. From this perspective, the active carbons gradually diffuse toward the Ni core. However, in these circumstances, the <sup>111</sup>In atoms located in these regions do not have enough energy to substitutionally diffuse into the Ni-fcc lattice, which are then housed in the Ni<sub>3</sub>C layer and at the interface between Ni<sub>3</sub>C and Ni-fcc.<sup>37,53</sup> Moreover, the higher content of active carbon during growth in nanoparticles synthesized with palm kernel oil along with the extensive

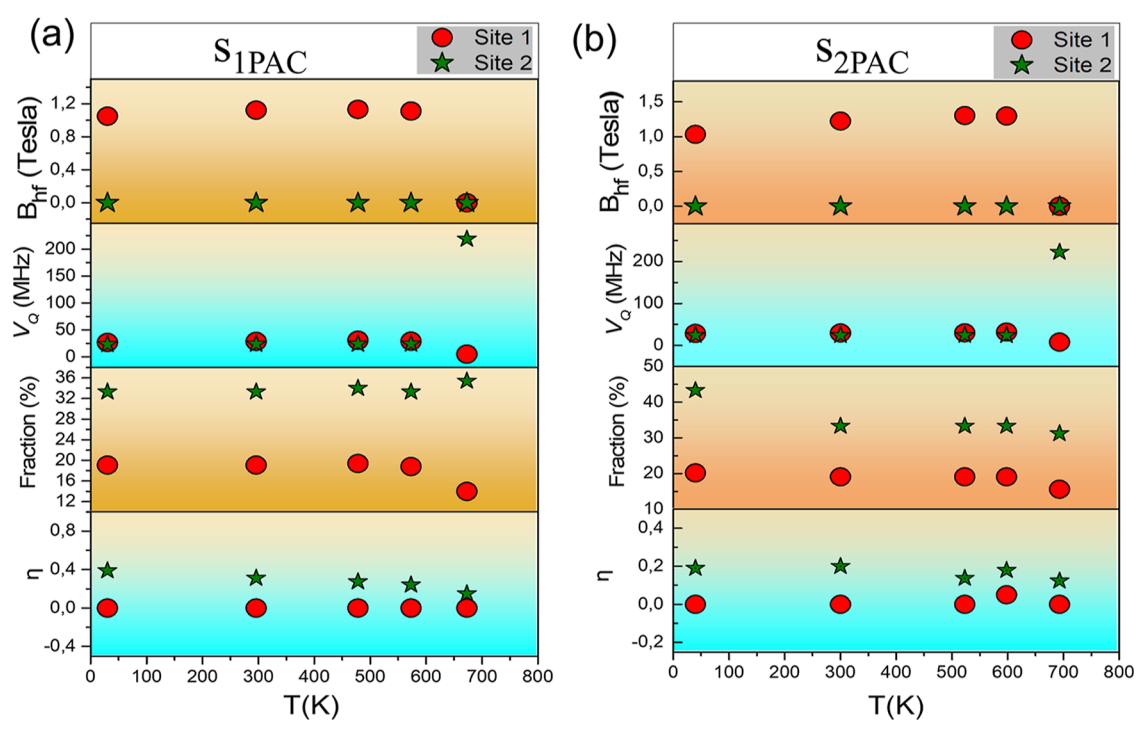


Figure 8. Hyperfine parameters extracted from the fit of the PAC results measured with the  $^{111}\text{In}(^{111}\text{Cd})$  probe nucleus in the range of 30–693 K. The parameters presented are the asymmetry parameter  $(\eta)$ , population of sites, quadrupole frequency  $(\nu_{\text{Q}})$ , and hyperfine magnetic field  $(B_{\text{hf}})$ . Parameters referring to the (a)  $S_{\text{1PAC}}$  and (b)  $S_{\text{2PAC}}$  samples. The parameters show approximately similar values for both samples, with significant changes being evidenced from 600 K, and these changes are compatible with the phase-transition changes observed in the R(t) spectra for both samples.

diffusibility of carbon in Ni compared to <sup>111</sup>In atoms hindered the diffusion of the probe in these samples. This resulted in a greater fraction of probes being accommodated in the coating regions. <sup>75,76</sup>

Taking into account the hyperfine parameters determined for the radioactive samples as well as the results obtained for the nonradioactive samples, a comparison between these findings and the predicted properties for Ni/Ni<sub>3</sub>C nanoparticles in the literature may clarify information about the hyperfine fields acting around the probes. The weak magnetic frequency obtained for site 1 ( $\nu_{\rm M1}$  = 2.25 MHz,  $B_{\rm hf}$  = 1 T) indicates probe nuclei located at the Ni/Ni<sub>3</sub>C interface in regions deficient in carbon since the presence of these regions is predicted in the literature during the structuring of nanoparticles due to imperfections in the carbon diffusion mechanism, which promotes the appearance of a weak magnetic field in Ni<sub>3</sub>C nanoparticles. 41,48 On the other hand, site 2, due to the absence of a hyperfine magnetic field ( $\nu_{O2}$  = 24 MHz,  $B_{\rm hf} = 0$ ), is representative of pure Ni<sub>3</sub>C (Figure 6c), which does not show ferromagnetic behavior due to strong hybridization between Ni and C, as anticipated in previous studies. 41,46 However, even though these results align with the literature, the XRD patterns presented in Figure 1 show subtle discrepancies, suggesting that samples synthesized using the oleylamine/oleic acid ligand pair present greater similarity to Ni-hcp compared with samples synthesized using the oleylamine/palm kernel oil ligand pair.

It is well known that measurements of hyperfine interactions are local "fingerprints", which, for instance, describe the crystalline symmetries around the probe nucleus. A number of questions are relevant for the outcomes of the hyperfine interactions, including: "Which charge configurations and

symmetries do these quadrupole frequencies represent?" In addition, could the observation of hyperfine interactions help to validate the resulting phase (Ni-hcp or  $Ni_3C$ )? Could they offer experimental evidence of the process by which these nanoparticles were formed?"

A methodology that has been used in recent years to validate the results of hyperfine interactions is first-principles calculations based on DFT, which simulate the position of the probe nucleus within crystalline symmetries. In this sense, Ferreira et al. utilized first-principles calculations to comprehend the electronic structure of Ce<sub>2</sub>O in the context of hyperfine interactions using the <sup>111</sup>In(<sup>111</sup>Cd) probe, indicating the presence of oxygen monovacancies in these structures.<sup>77</sup> From this approach, first-principles calculations were conducted to enhance our understanding of the previously presented hyperfine interaction results.

**2.2. Ab Initio Calculations.** First-principles calculations based on DFT were performed to investigate the location of the probe nuclei. These calculations simulate Cd atoms replacing Ni atoms in different crystalline environments (Nifcc and Ni-hcp). In the simulations, performed using the WIEN2k package, <sup>78</sup> a DFT implementation with APW + lo base functions was used. The results of these calculations for the Ni-fcc phase were  $V_{zz} = 0$  and  $B_{hf} = -6.01$  T. These results are in good agreement with the experimental results for the Ni<sub>WPAC</sub> sample (metallic wire of Ni with high purity), which are  $B_{hf} = 7.1(1)$  T and  $V_z = 0$ .

In contrast, the results of the  $^{111}$ Cd calculations in the Nihcp phase show a quadrupole frequency of  $nu_{Q1} = 29.1$  MHz with a hyperfine field of  $B_{hf} = 5.5$  T. Although these data reveal a  $nu_Q$  value that quite agrees with the value obtained from the fit of spectra for site 1, the  $B_{hf}$  value for this site is inconsistent.

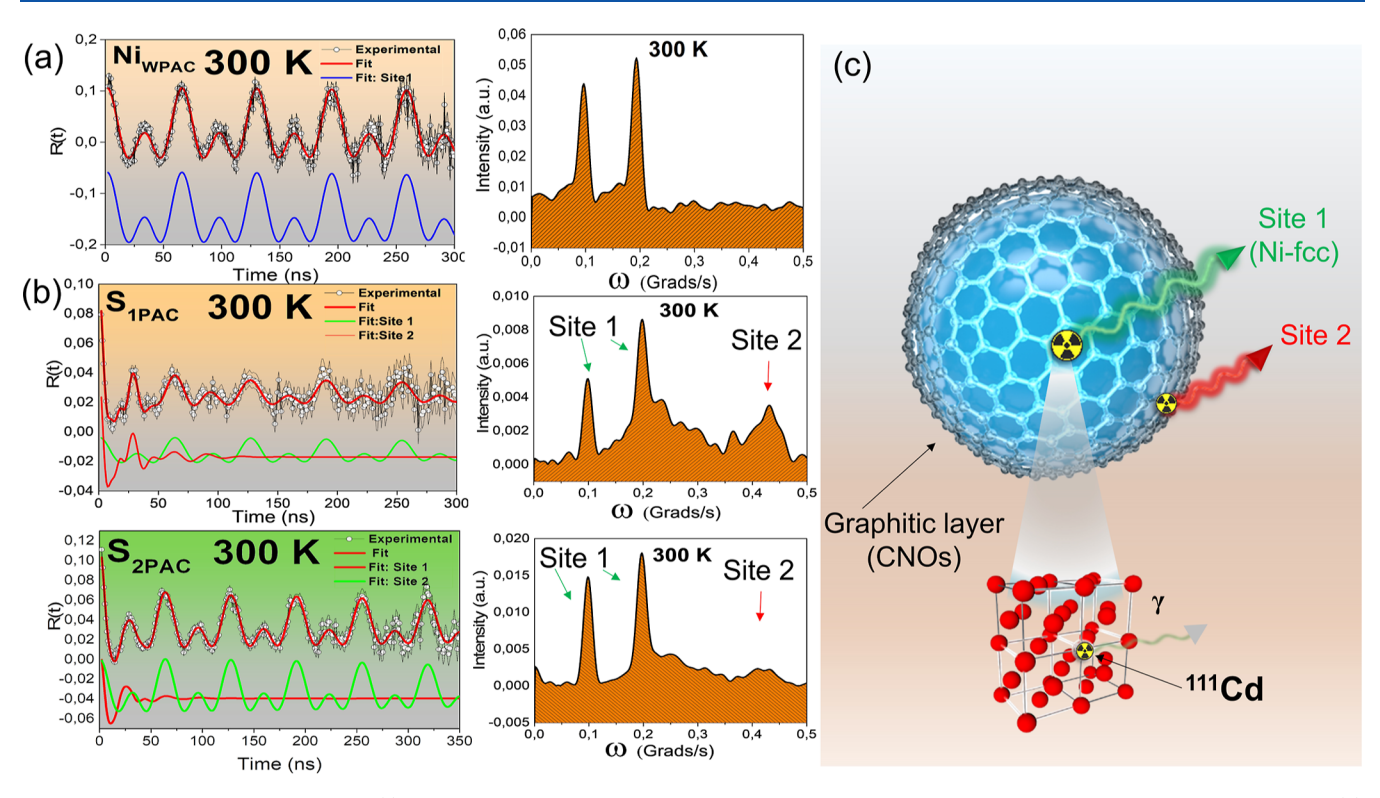


Figure 9. Anisotropy ratio functions R(t) and their corresponding FFTs obtained at 300 K after annealing in a nitrogen atmosphere at 700 K. (a) Ni<sub>WPAC</sub> (Ni-fcc wire). (b) S<sub>1PAC</sub> and S<sub>2PAC</sub> (nanoparticles synthesized using oleic acid and palm kernel oil, respectively). A comparative evaluation of the spectra indicates a predominance of substitutional <sup>111</sup>In(<sup>111</sup>Cd) in the Ni-fcc lattice, observed in all samples and denoted site 1 for the nanoparticle samples. In addition to this site, another site is observed in the S<sub>1PAC</sub> and S<sub>2PAC</sub> samples, called site 2, which may be associated with the probe nuclei at the interface region between Ni-fcc and the CNOs. (c) Schematic representation of the location of the nuclei in the nanoparticles.

These findings indicate that the Ni-hcp phase does not form in either sample of nanoparticles. This implies that the PAC results correspond indeed to the Ni<sub>3</sub>C phase, as explained above for nonradioactive samples, which is consistent with the literature, where recent works have used different methodologies to demonstrate the formation of this phase in wet synthesis routes that use metal salts and solvents such as oleylamine and oleic acid.

**2.3. Phase Transformations Observed in Radioactive Samples.** As discussed in previous sections, XRD results for the nonradioactive nanoparticles suggest an evident influence of reducing agents on the Ni<sub>3</sub>C content, whereas DSC results during annealing under a nitrogen atmosphere show their decomposition into 3Ni(s) and C at 695 K. Additionally, the TEM measurements after annealing indicate that formation of CNOs can be influenced by the carbon content in these nanoparticles. These observed occurrences were then investigated by hyperfine interactions in a wide range of temperatures from 30 to 693 K.

Figure 7 show the perturbation spectra R(t) and its FFTs, which are similar for both samples. Until 600 K, spectra for both samples  $S_{1PAC}$  and  $S_{2PAC}$ , displayed, respectively, in Figure 7a,b, show the same modulation, which modifies appreciably above this temperature, with a strong and predominant cubic contribution, which could be a sign of a change in the crystalline environment.<sup>71</sup> These results demonstrate the local stability of the nanoparticles over time below the transition temperature. This characteristic is particularly important considering that the acquisition of each experimental spectrum required a period of 12 h (as shown in the Methods).

The temperature dependence of the hyperfine parameters provides the best illustration of the evident phase transition in the R(t) functions above 600 K. Changes at sites 1 and 2 with temperature variation are depicted in Figure 8. The hyperfine parameters obtained for both samples show significant agreement with each other, as shown in Figure 8a,b. Site 1 is characterized by a quadrupole frequency of around 28 MHz, with a contribution of a weak magnetic frequency ( $\sim$ 2.4 MHz) for temperatures below 600 K. For site 2, in this range of temperatures, only one quadrupole frequency of around 24 MHz is obtained, with no magnetic contribution. An interesting observation refers to the asymmetry parameter for both samples. As seen in Figure 8, site 1 in both samples has a null asymmetry parameter ( $\eta = 0$ ), but for site 2, these parameters are not null, suggesting probable distortions in the regions surrounding the probe nuclei. Given that the carbon diffusion mechanism is not perfect, these distortions may be related to the amount of carbon present in the lattice. However, the higher carbon content of nanoparticles made from palm kernel oil  $(S_{2PAC})$  may increase the occurrence of these distortions, which would account for the increased asymmetry seen in these samples.

The modulations in R(t) that occur at temperatures above 600 K, observed in Figure 7, are illustrative of the alterations in the hyperfine interactions due to the phase transition. In both samples, above this temperature, a decrease in the quadrupole frequency of site 1 and a significant increase in the quadrupole frequency of site 2 are observed (Figure 8). No magnetic frequency was detected above this temperature because under these conditions Ni loses its ferromagnetic character, which implies  $B_{\rm hf} = 0$  as previously reported.<sup>42</sup>

Quadrupole frequency variations could clarify the carbon diffusion process underlying Ni<sub>3</sub>C decomposition. The decrease in the quadrupole frequency for site 1 associated with the Ni/Ni<sub>3</sub>C interface indicates that only the carbon atoms migrate from the Ni<sub>3</sub>C interstices to the surface and grain boundaries of the nanoparticles. However, because this temperature is insufficient to promote the diffusion of Cd atoms, the <sup>111</sup>In(<sup>111</sup>Cd) probes continue to replace the nickel atoms above 600 K. The crystalline environment of the Ni-fcc phase is "cleaned" by the diffusion of carbon out of the nanoparticles. The increase in the quadrupole frequency (~230 MHz) for site 2, establishing the formation of graphite around the nanoparticles, confirms that the generation of CNOs occurs during the annealing process and not exclusively by precipitation after cooling.<sup>21</sup>

After thermal treatment at 700 K for the nanoparticles  $(S_{1PAC} \text{ and } S_{2PAC})$ , new PAC measurements were taken at room temperature (300 K). Figure 9 shows the R(t) functions and their corresponding FFTs. Figure 9a displays R(t) for the Ni<sub>WPAC</sub> sample measured at 300 K for comparative purposes. Figure 9b refers to the R(t) values measured for thermally treated S<sub>1PAC</sub> and S<sub>2PAC</sub> samples. For the nanoparticles, the functions obtained are characteristic of <sup>111</sup>In(<sup>111</sup>Cd) in a Ni-fcc environment, as observed for the Ni<sub>WPAC</sub> sample. The Ni-fcc site in the nanoparticles, called site 1, has, for both samples ( $S_{1PAC}$  and  $S_{2PAC}$ ), a well-defined magnetic frequency ( $\nu_{M1}$  = 15.50 MHz), with an associated magnetic hyperfine field of  $\sim$ 6 T, a frequency distribution of  $\delta_1$  = 0.01 MHz, and an asymmetry parameter  $\eta = 0$ . However, in addition to the characteristic Ni-fcc site, a second site was detected, with a high quadrupole frequency  $\nu_{\rm Q2}\sim 230$  MHz and a high magnetic frequency  $\nu_{\rm M2}\sim 3.4$  MHz associated with a hyperfine magnetic field  $B_{\rm hf}=1.4$  T, with frequency distribution  $\delta_2=0.1$ MHz and asymmetry parameter  $\eta = 0.3$ , called site 2. Although the quadrupole frequency predicted in the literature for <sup>111</sup>In(<sup>111</sup>Cd) in graphite is 270 MHz, <sup>79</sup> the Ni atoms present in the surroundings of the probe nuclei in the interface region between Ni and graphite may contribute to the decrease in the quadrupole frequency and concomitant appearance of a weak hyperfine magnetic field.

# 3. CONCLUSIONS

In the current investigation, we present the thermal decomposition-based synthesis of Ni/Ni<sub>3</sub>C core-shell nanoparticles using two distinct ligand pairs (oleylamine/oleic acid and oleylamine/palm kernel oil). XRD, TEM, TGA/DSC, magnetic measurements, and a nuclear local technique were used to study how these ligands influence the properties of the nanoparticles. The findings support the viability of synthesis using both ligand pairs, suggesting that the utilization of palm kernel oil leads to a higher proportion of Ni<sub>3</sub>C, a broader size distribution, and a lower saturation magnetization of nanoparticles compared to that of oleic acid. Local inspection in the 30-40 K temperature range along with first-principles calculation methodology pointed out the formation of Ni<sub>3</sub>C regions and Ni<sub>3</sub>C regions with carbon deficiency, featuring a magnetic hyperfine field of 1 T, and revealed the absence of the Ni-hcp phase in both types of samples. Additionally, thermal analysis results showed that the samples underwent a phase change at 695 K, which indicated the decomposition of the Ni<sub>3</sub>C layer into Ni and C. After annealing, Ni-fcc nanoparticles encapsulated in CNOs were observed in the TEM/EDS results. The findings suggest that a higher Ni<sub>3</sub>C content in

these nanoparticles is a factor in the formation of NOs with more layers. The stability of Ni/Ni3C at temperatures below the transition temperature is clearly shown by local investigation as a function of temperature. Beyond this temperature (695 K), changes in the modulation of PAC spectra and, as a result, hyperfine parameters were observed. These changes suggest the occurrence of carbon migration to the nanoparticle surface, forming CNOs as the annealing process continues. After the solution was cooled, local measurements confirmed the formation of Ni-fcc and CNOs, indicating the existence of a weak magnetic field at the interface between these structures. Thus, the use of palm kernel oil as a ligand for the formation of Ni/Ni3C nanoparticles is relevant, especially given the promising role that these systems have in catalyzing the growth of Ni nanoparticles encapsulated in CNOs, which are of great interest for electrocatalytic applications in processes such as HER and OER.

## 4. METHODS

4.1. Synthesis of Samples. Nanoparticles were synthesized using the thermal decomposition method described by Chiang et al.<sup>3</sup> Nickel(II) acetylacetonate (Ni(acac)2, Merck, 98%) was used as a metallic precursor in the process, and oleylamine (Merck, 70%) and oleic acid (Labsynth, >98%) were used as the solvent and ligand pair, respectively. The latter pair was also replaced by oleylamine/palm kernel oil. Palm kernel oil was provided by the extraction laboratory (LABEX/UFPA); it was obtained by the supercritical CO<sub>2</sub> extraction method at 40 °C and 150 bar and contained 79.36% saturated fatty acids, with a higher proportion of lauric acid (C12:0).66 In this route, oleylamine acted as a reducing agent, and the secondary ligand acted as a surfactant. Thus, 500 mg of Ni(acac)2, 36 mL of oleylamine, and 4 mL of oleic acid or palm kernel oil were placed in a three-neck flask, and the solution was homogenized by sonication. After homogenization, the solution was heated to 170 °C (443 K) at a heating rate of 10 °C min<sup>-1</sup> and kept at this temperature, under a nitrogen atmosphere, for 10 min for nucleation of the nanoparticles. Subsequently, the temperature was increased to 240 °C (513 K) for the growth stage, where it remained for 3 h, under constant reflux. After this step, the nanoparticles were separated by centrifugation at 7000 rpm for 20 min and washed with toluene, acetone, and isopropanol separately. The precipitate was dried under low pressure (about 1 kPa) for 24 h, and a powder was obtained.

To perform PAC measurements, it is necessary to introduce radioactive probe nuclei into the structure of the material to be studied. In our work,  $^{111} \mathrm{In}(^{111}\mathrm{Cd})$  was used, which is one of the most used probe nuclei due to its excellent nuclear properties and radioactive characteristics of the  $^{111}\mathrm{In}$  parent nucleus  $^{80}$  that decays via electron capture to  $^{111}\mathrm{Cd}$ . Thus, hereafter, the probe nucleus will be represented as  $^{111}\mathrm{In}(^{111}\mathrm{Cd})$ .

Measurements of PAC experiments yield the time-dependent anisotropy ratio function  $R(t) = A_{22} \sum_i f_i G_{22}^i(t)$ , which can be fitted by a model that takes into account the population (f) of probe nuclei in different environments (fractional sites) and their respective perturbation function  $G_{22}(t)$ .  $A_{22}$  is the angular correlation coefficient, which, for  $^{111} {\rm In}(^{111} {\rm Cd})$  is  $-0.18,^{81}$  and because it is negative, the R(t) functions are displayed with the y axis inverted.

The perturbation function for magnetic hyperfine interactions is given by  $G_{22}(t) = 0.2 + 0.4 \sum_{n=1,2} \cos(n\omega_{\rm L}t)$ , and its measurement allows the determination of the Larmor frequency  $\omega_{\rm L} = \mu_{\rm N} g B_{\rm hf}/\hbar$ , where  $\mu_{\rm N}$  is the nuclear magnetron and g is the nuclear g-factor, and then the calculation of the magnetic hyperfine field  $B_{\rm hf}$ .

then the calculation of the magnetic hyperfine field  $B_{\rm hf}$ . For electric quadrupole interactions,  $G_{22}(t) = S_{20} + \sum_{n=1,2,3} S_{2n}(\eta) \cos(n\omega_n t)$ , where the transition frequencies  $\omega_n = g_n(\eta)\nu_Q$  are proportional to the quadrupole frequency  $\nu_Q = eQV_{zz}/h$ , and, along with the  $S_{2n}$  coefficients, depend on the asymmetry parameter  $\eta = (V_{xx} - V_{yy})/V_{zz}$ . PAC experiments determine the quadrupole frequency  $\nu_Q$ 

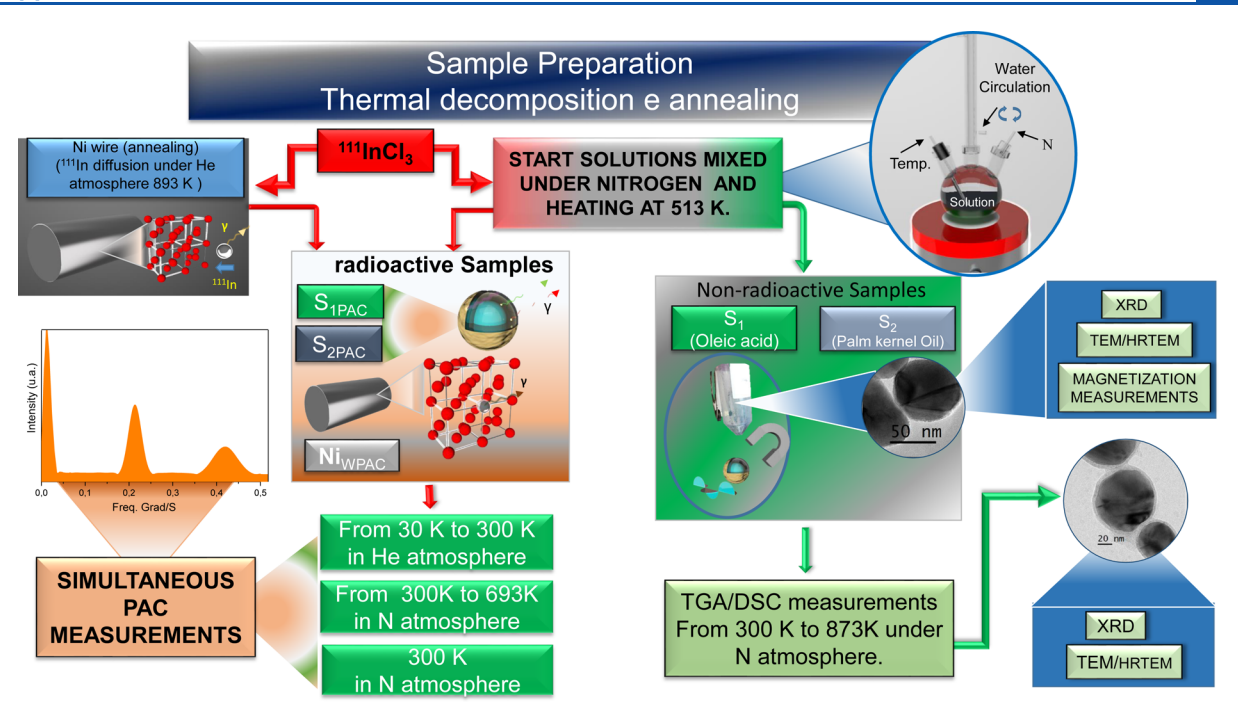


Figure 10. Schematic picture showing the steps involved in preparing and characterizing radioactive and nonradioactive samples using PAC, XRD, TEM/HRTEM, and thermal analysis (TGA/DSC). The PAC data, which cover the 30–693 K temperature range, are typical of the group of radioactive samples. Rest of the characterizations are typical of the nonradioactive samples, whose synthesis details are equal to those of the radioactive samples (see text).

and  $\eta$ , allowing the calculation of the  $V_{kk}$ , k = x, y, z, components of the electric-field-gradient tensor, since the quadrupole moment Q of the probe nucleus is known. The nuclear quadrupole moment for the 245 keV level of  $^{111}$ Cd was recently reported as Q = 0.76 b by Errico et al.<sup>82</sup> and agrees very well with the value of 0.765 b previously reported by Haas and Correa. 83 The major component  $(V_{zz})$  of EFG, calculated from the experimentally measured  $\nu_{Q}$ , as well as the measure of  $\eta$ , provide information about the configuration of the electric field gradient in the crystallographic site where the probe nuclei are located. The parameter  $\eta$ , with values limited to  $0 \le \eta \le 1$ , thus quantifies the deviation from axial symmetry of the local charge distribution due to local distortion of the crystallographic site.8 Furthermore, it is important to emphasize that  $\eta$  provides information on the local symmetry, whereas  $V_{zz}$  provides information on the charge density surrounding the probe nucleus. Additional information on PAC technique can be found elsewhere.85

In PAC experiments, there are different routes for introducing radioactive nuclei as a diluted impurity in systems such as nanoparticles, thin films, or bulk: by implantation, <sup>86</sup> by thermal diffusion, <sup>87</sup> during melting or synthesis, <sup>88,89</sup> and by a nuclear reaction during irradiation of the sample. 90,91 In this work, the probe nuclei were inserted through the addition of a small volume of radioactive InCl<sub>3</sub> during the synthesis of nanoparticles. Moreover, in order to obtain comparative parameters, we tried to investigate how the probe nucleus would behave in a Ni-fcc environment. For this, 111 In probes were thermally diffused on a high-purity nickel wire (99,999%). In the process, the Ni wire was immersed in an InCl<sub>3</sub> solution, dried, and then placed within a quartz tube. The quartz tube was evacuated and sealed in a low He atmosphere and then heated at 893 K for 12 h. The samples were divided into two groups, the radioactive sample group and the nonradioactive sample group, for characterization. Both groups contain nanoparticles made of oleic acid, nanoparticles made of palm kernel oil, and pure Ni wire. The nonradioactive samples were called samples S<sub>1</sub>, S<sub>2</sub>, and Ni<sub>W</sub>, respectively. Whereas S<sub>1PAC</sub>, S<sub>2PAC</sub>, and Ni<sub>WPAC</sub> samples comprised a set of radioactive samples, which were all created using the same method as nonradioactive samples.

**4.2. Characterization of Samples.** The radioactive samples were individually placed in the sample holder of a helium closed-cycle

refrigerator to carry out measurements in the range of 30-300 K for the characterization using PAC. These observations were made in order to better understand how the samples behave at low temperatures. After measurement at low temperatures, the nanoparticle samples (S<sub>1PAC</sub> and S<sub>2PAC</sub>) were sealed in a quartz tube under low nitrogen pressure (about 0.2 atm) and placed inside a small oven to perform PAC measurements during annealing, in the range 300 to 693 K. Each measurement lasted for 12 h, at which point the R(t)functions were obtained. After measurement at the highest temperature (693 K), the system was cooled to room temperature, and the R(t) was obtained to verify if any transitions occurred after annealing. All PAC results were obtained using the PAC spectrometer with four BaFe2 detectors at the Laboratory of Hyperfine Interactions of the Nuclear and Energy Research Institute (IPEN), São Paulo, Brazil. Details on the experimental procedure for PAC measurements can be found elsewhere.

For the group of nonradioactive samples, the size distribution and morphology of samples  $S_1$  and  $S_2$  were determined by transmission electron microscopy (TEM) measurements, while the crystalline structure was determined using X-ray diffraction (XRD). For the magnetic characterization of the samples, magnetization measurements were carried out with an applied field. To verify possible phase transitions, thermal analysis measurements (thermogravimetric analysis/differential scanning calorimetry—TGA/DSC) were carried out for both samples in the range of 30–600 °C (300–873 K), with a heating rate of 10 °C·min<sup>-1</sup>, under a nitrogen flow of 100 mL·min<sup>-1</sup>. The crystalline structure and morphology of the samples were checked again after thermal analysis by XRD and TEM/HRTEM. Figure 10 presents a systematic description of the procedures adopted for both groups of samples (for additional experimental details of the characterization techniques used, see the Supporting Information).

## ASSOCIATED CONTENT

# Supporting Information

The Supporting Information is available free of charge at https://pubs.acs.org/doi/10.1021/acsanm.3c03205.

Additional characterization data, including FTIR spectra for the samples and images of HRTEM (PDF)

#### AUTHOR INFORMATION

# **Corresponding Authors**

Artur W. Carbonari — Instituto de Pesquisas Energéticas e Nucleares IPEN-CNEN/SP, São Paulo 05508-000 SP, Brazil; ⊚ orcid.org/0000-0002-4499-5949;

Email: carbonar@ipen.br

Larissa Otubo — Instituto de Pesquisas Energéticas e Nucleares IPEN-CNEN/SP, São Paulo 05508-000 SP, Brazil;

Email: larissa.otubo@ipen.br

#### **Authors**

Crystian W. C. Silva — Instituto de Pesquisas Energéticas e Nucleares IPEN-CNEN/SP, São Paulo 05508-000 SP, Brazil

Gabriel A. Cabrera-Pasca — Faculty of Exacts Sciences and Technology, Federal University of Pará, Abaetetuba 684440-000 PA, Brazil

Katiusse S. Souza – Instituto de Pesquisas Energéticas e Nucleares IPEN-CNEN/SP, São Paulo 05508-000 SP, Brazil

Cleidilane S. Costa – Faculty of Exacts Sciences and Technology, Federal University of Pará, Abaetetuba 684440-000 PA, Brazil

Messias S. Costa — Faculty of Exacts Sciences and Technology, Federal University of Pará, Abaetetuba 684440-000 PA, Brazil; orcid.org/0000-0001-6087-2810

Bruno S. Correa — Instituto de Pesquisas Energéticas e Nucleares IPEN-CNEN/SP, São Paulo 05508-000 SP, Brazil

Wanderson L. Ferreira — Instituto de Pesquisas Energéticas e Nucleares IPEN-CNEN/SP, São Paulo 05508-000 SP, Brazil

Rafael S. Freitas – Institute of Physics, IFUSP, University of São Paulo, São Paulo 05508-090 SP, Brazil

Complete contact information is available at: https://pubs.acs.org/10.1021/acsanm.3c03205

#### Notes

The authors declare no competing financial interest.

## ACKNOWLEDGMENTS

A.W.C. acknowledges the financial support received from Conselho Nacional de Desenvolvimento Científico e Tecnológico (CNPq) and Fundação de Amparo a Pesquisa do Estado de São Paulo (FAPESP) under grants 304627/2017-8 and grants 2014/14001-1 and 2017/50332-0, respectively, as well as from the Instituto de Pesquisas Energéticas e Nucleares IPEN-CNEN/SP for financial support under projects 2020.06.IPEN.43 and 2020.06.IPEN.38. G.A. Cabrera-Pasca gratefully acknowledges support of the RCGI-Research Centre for Greenhouse Gas Innovation, hosted by the University of São Paulo (USP) and sponsored by FAPESP— São Paulo Research Foundation (2014/50279-4 and 2020/ 15230-5) and Shell Brasil, and the strategic importance of the support given by ANP (Brazil's National Oil, Natural Gas and Biofuels Agency) through the R&D levy regulation. The authors thank the Extraction Laboratory (LABEX/UFPA) for donating the palm kernel oil.

#### REFERENCES

- (1) Zhang, D.; Zhang, C.; Liu, J.; Chen, Q.; Zhu, X.; Liang, C. Carbon-Encapsulated Metal/Metal Carbide/Metal Oxide Core—Shell Nanostructures Generated by Laser Ablation of Metals in Organic Solvents. ACS Appl. Nano Mater. 2019, 2 (1), 28–39.
- (2) Wang, H.; Xiong, J.; Cheng, X.; Fritz, M.; Ispas, A.; Bund, A.; Chen, G.; Wang, D.; Schaaf, P. Ni<sub>3</sub>N-Coated Ni Nanorod Arrays for Hydrogen and Oxygen Evolution in Electrochemical Water Splitting. *ACS Appl. Nano Mater.* **2020**, *3* (11), 10986–10995.
- (3) Xiong, L.; Fu, Y.; Luo, Y.; Wei, Y.; Zhang, Z.; Wu, C.; Luo, S.; Wang, G.; Sawtell, D.; Xie, K.; Wu, T.; Ding, D.; Huang, L. Prospective Applications of Transition Metal—Based Nanomaterials. *J. Mater. Res.* 2022, 37 (13), 2109–2123.
- (4) Du, H.; Akakuru, O. U.; Yao, C.; Yang, F.; Wu, A. Transition Metal Ion-Doped Ferrites Nanoparticles for Bioimaging and Cancer Therapy. *Transl. Oncol.* **2022**, *15* (1), 101264.
- (5) Correa, B. S.; Costa, M. S.; Cabrera-Pasca, G. A. G. A.; Sena, C.; Holanda Pinto, R. H.; Silva, A. P. S.; Carvalho Junior, R. N.; Ishida, L.; Ramon, J. G. A.; Freitas, R. S.; Saiki, M.; Matos, I. T.; Corrêa, E. L.; Carbonari, A. W. High-saturation magnetization in small nanoparticles of Fe<sub>3</sub>O<sub>4</sub> coated with natural oils. *J. Nanoparticle Res.* **2020**, *22*, *68*.
- (6) Xiao, Y.; Sun, P.; Cao, M. Core—Shell Bimetallic Carbide Nanoparticles Confined in a Three-Dimensional N-Doped Carbon Conductive Network for Efficient Lithium Storage. ACS Nano 2014, 8 (8), 7846—7857.
- (7) Xiao, Y.; Hwang, J.-Y.; Sun, Y.-K. Transition Metal Carbide-Based Materials: Synthesis and Applications in Electrochemical Energy Storage. *J. Mater. Chem. A* **2016**, *4* (27), 10379–10393.
- (8) Qie, Y.; Liu, Y.; Kong, F.; Yang, Z.; Yang, H. High Coercivity Cobalt Carbide Nanoparticles as Electrocatalysts for Hydrogen Evolution Reaction. *Nano Res.* **2022**, *15* (5), 3901–3906.
- (9) Khurshid, H.; Abdu, Y. A.; Devlin, E.; Issa, B. A.; Hadjipanayis, G. C. Chemically Synthesized Nanoparticles of Iron and Iron-Carbides. RSC Adv. 2020, 10 (48), 28958–28964.
- (10) Yue, Q.; Wan, Y.; Sun, Z.; Wu, X.; Yuan, Y.; Du, P. MoP Is a Novel, Noble-Metal-Free Cocatalyst for Enhanced Photocatalytic Hydrogen Production from Water under Visible Light. *J. Mater. Chem.* A **2015**, 3 (33), 16941–16947.
- (11) Fang, L. J.; Wang, X. L.; Li, Y. H.; Liu, P. F.; Wang, Y. L.; Zeng, H. D.; Yang, H. G. Nickel Nanoparticles Coated with Graphene Layers as Efficient Co-Catalyst for Photocatalytic Hydrogen Evolution. *Appl. Catal., B* **2017**, 200, 578–584.
- (12) Jiao, M.; Li, K.; Guan, W.; Wang, Y.; Wu, Z.; Page, A.; Morokuma, K. Crystalline Ni<sub>3</sub>C as Both Carbon Source and Catalyst for Graphene Nucleation: A QM/MD Study. *Sci. Rep.* **2015**, *5* (1), 12091.
- (13) Ürk, D.; Cebeci, F. Ç.; Öveçoğlu, M. L.; Cebeci, H. Structure-Controlled Growth of Vertically-Aligned Carbon Nanotube Forests Using Iron—Nickel Bimetallic Catalysts. *Mater. Adv.* **2021**, 2 (6), 2021–2030.
- (14) Turaeva, N.; Kuljanishvili, I. Effects of Electronic Structure of Catalytic Nanoparticles on Carbon Nanotube Growth. *Carbon Trends* **2021**, *5*, 100092.
- (15) Vindhyasarumi, A.; Anjali, K. P.; Sethulekshmi, A. S.; S Jayan, J.; Deeraj, B.; Saritha, A.; Joseph, K. A Comprehensive Review on Recent Progress in Carbon Nano-Onion Based Polymer Nano-composites. *Eur. Polym. J.* **2023**, *194*, 112143.
- (16) Dong, T.; Zhang, X.; Cao, Y.; Chen, H.-S.; Yang, P. Ni/Ni<sub>3</sub>C Core—Shell Nanoparticles Encapsulated in N-Doped Bamboo-like Carbon Nanotubes towards Efficient Overall Water Splitting. *Inorg. Chem. Front.* **2019**, *6* (4), 1073–1080.
- (17) Goldie, S. J.; Jiang, S.; Coleman, K. S. Cobalt Nanoparticle Catalysed Graphitization and the Effect of Metal Precursor Decomposition Temperature. *Mater. Adv.* **2021**, *2* (10), 3353–3361.
- (18) Munir, A.; Haq, T. u.; Saleem, M.; Qurashi, A.; Hussain, S. Z.; Sher, F.; Ul-Hamid, A.; Jilani, A.; Hussain, I. Controlled Engineering of Nickel Carbide Induced N-Enriched Carbon Nanotubes for

- Hydrogen and Oxygen Evolution Reactions in Wide PH Range. *Electrochim. Acta* **2020**, 341, 136032.
- (19) Khoshk Rish, S.; Tahmasebi, A.; Wang, R.; Dou, J.; Yu, J. Formation Mechanism of Nano Graphitic Structures during Microwave Catalytic Graphitization of Activated Carbon. *Diam. Relat. Mater.* **2021**, *120*, 108699.
- (20) Mykhailiv, O.; Zubyk, H.; Plonska-Brzezinska, M. E. Carbon Nano-Onions: Unique Carbon Nanostructures with Fascinating Properties and Their Potential Applications. *Inorg. Chim. Acta* **2017**, 468, 49–66.
- (21) Goldie, S. J.; Coleman, K. S. Graphitization by Metal Particles. ACS Omega 2023, 8 (3), 3278–3285.
- (22) Ahlawat, J.; Masoudi Asil, S.; Guillama Barroso, G.; Nurunnabi, M.; Narayan, M. Application of Carbon Nano Onions in the Biomedical Field: Recent Advances and Challenges. *Biomater. Sci.* **2021**, 9 (3), 626–644.
- (23) Frasconi, M.; Maffeis, V.; Bartelmess, J.; Echegoyen, L.; Giordani, S. Highly Surface Functionalized Carbon Nano-Onions for Bright Light Bioimaging. *Methods Appl. Fluoresc.* **2015**, *3* (4), 044005.
- (24) Thambiliyagodage, C. J.; Ulrich, S.; Araujo, P. T.; Bakker, M. G. Catalytic Graphitization in Nanocast Carbon Monoliths by Iron, Cobalt and Nickel Nanoparticles. *Carbon* **2018**, *134*, 452–463.
- (25) Gomez-Martin, A.; Schnepp, Z.; Ramirez-Rico, J. Structural Evolution in Iron-Catalyzed Graphitization of Hard Carbons. *Chem. Mater.* **2021**, 33 (9), 3087–3097.
- (26) Barman, B. K.; Nanda, K. K. Prussian Blue as a Single Precursor for Synthesis of Fe/Fe<sub>3</sub>C Encapsulated N-Doped Graphitic Nanostructures as Bi-Functional Catalysts. *Green Chem.* **2016**, *18* (2), 427–432.
- (27) Gao, D.; Zhang, J.; Wang, T.; Xiao, W.; Tao, K.; Xue, D.; Ding, J. Metallic Ni<sub>3</sub>N Nanosheets with Exposed Active Surface Sites for Efficient Hydrogen Evolution. *J. Mater. Chem. A* **2016**, *4* (44), 17363–17369.
- (28) Shahroudi, A.; Esfandiari, M.; Habibzadeh, S. Nickel Sulfide and Phosphide Electrocatalysts for Hydrogen Evolution Reaction: Challenges and Future Perspectives. *RSC Adv.* **2022**, *12* (45), 29440–29468
- (29) Sivagami, M.; Asharani, I. V. Phyto-Mediated Ni/NiO NPs and Their Catalytic Applications-a Short Review. *Inorg. Chem. Commun.* **2022**, *145*, 110054.
- (30) Tahmasebi, S.; Jahangiri, S.; Mosey, N.; Jerkiewicz, G.; Mark, A.; Cheng, S.; Botton, G.; Baranton, S.; Coutanceau, C. Remarkably Stable Nickel Hydroxide Nanoparticles for Miniaturized Electrochemical Energy Storage. *ACS Appl. Energy Mater.* **2020**, 3 (8), 7294–7305
- (31) Qin, Q.; Hao, J.; Zheng, W. Ni/Ni<sub>3</sub>C Core/Shell Hierarchical Nanospheres with Enhanced Electrocatalytic Activity for Water Oxidation. ACS Appl. Mater. Interfaces 2018, 10, 17827–17834.
- (32) Kumar, R.; Kumar, A.; Verma, N.; Khopkar, V.; Philip, R.; Sahoo, B. Ni Nanoparticles Coated with Nitrogen-Doped Carbon for Optical Limiting Applications. *ACS Appl. Nano Mater.* **2020**, 3 (9), 8618–8631.
- (33) Zhang, X.; Zhang, K.; Zhang, W.; Zhang, X.; Wang, L.; An, Y.; Sun, X.; Li, C.; Wang, K.; Ma, Y. Carbon Nano-Onion-Encapsulated Ni Nanoparticles for High-Performance Lithium-Ion Capacitors. *Batteries* **2023**, *9* (2), 102.
- (34) Singh, V. Natural Source Derived Carbon Nano-Onions as Electrode Material for Sensing Applications. *Diam. Relat. Mater.* **2018**, 87, 202–207.
- (35) Ghalkhani, M.; Khosrowshahi, E. M.; Sohouli, E. *Handbook of Carbon-Based Nanomaterials*; Elsevier, 2021, pp 159–207..Carbon Nano-Onions: Synthesis, Characterization, and Application
- (36) Chiang, R.-T.; Chiang, R.-K.; Shieu, F.-S. Emergence of interstitial-atom-free HCP nickel phase during the thermal decomposition of Ni<sub>3</sub>C nanoparticles. *RSC Adv.* **2014**, *4*, 19488–19494.
- (37) Zhou, W.; Zheng, K.; He, L.; Wang, R.; Guo, L.; Chen, C.; Han, X.; Zhang, Z. Ni/Ni<sub>3</sub>C Core—Shell Nanochains and Its Magnetic Properties: One-Step Synthesis at Low Temperature. *Nano Lett.* **2008**, *8*, 1147—1152.

- (38) Gao, F.; Yang, Y.; Qiu, W.; Song, Z.; Wang, Q.; Niu, L. Ni<sub>3</sub>C/Ni Nanochains for Electrochemical Sensing of Glucose. *ACS Appl. Nano Mater.* **2021**, *4*, 8520–8529.
- (39) Zhu, Y.; Zhang, Y.; Wang, K.; Li, D.; Ding, F.; Meng, D.; Wang, X.; Zhang, Z. One-pot synthesis of Ni/Ni<sub>3</sub>C/Ni<sub>3</sub>N nanocomposite: Structure, growth mechanism and magnetic properties. *Mater. Res. Bull.* **2017**, *95*, 79–85.
- (40) Chen, Y.; Peng, D.-L.; Lin, D.; Luo, X. Preparation and magnetic properties of nickel nanoparticles via the thermal decomposition of nickel organometallic precursor in alkylamines. *Nanotechnology* **2007**, *18* (50), 505703.
- (41) Schaefer, Z. L.; Weeber, K. M.; Misra, R.; Schiffer, P.; Schaak, R. E. Bridging hcp-Ni and Ni $_3$ C via a Ni $_3$ C $_{1-x}$  Solid Solution: Tunable Composition and Magnetism in Colloidal Nickel Carbide Nanoparticles. *Chem. Mater.* **2011**, 23, 2475–2480.
- (42) He, X.; Zhong, W.; Au, C. T.; Du, Y. Size dependence of the magnetic properties of Ni nanoparticles prepared by thermal decomposition method. *Nanoscale Res. Lett.* **2013**, *8*, 446.
- (43) Mourdikoudis, S.; Menelaou, M.; Fiuza-Maneiro, N.; Zheng, G.; Wei, S.; Pérez-Juste, J.; Polavarapu, L.; Sofer, Z. Oleic acid/oleylamine ligand pair: a versatile combination in the synthesis of colloidal nanoparticles. *Nanoscale Horiz.* **2022**, *7*, 941–1015.
- (44) Harris, R. A.; Shumbula, P. M.; van der Walt, H. Analysis of the Interaction of Surfactants Oleic Acid and Oleylamine with Iron Oxide Nanoparticles through Molecular Mechanics Modeling. *Langmuir* **2015**, *31*, 3934–3943.
- (45) He, L. Hexagonal close-packed nickel or Ni<sub>3</sub>C? *J. Magn. Magn. Mater.* **2010**, 322, 1991–1993.
- (46) Fang, C. M.; Sluiter, M. H. F.; van Huis, M. A.; Zandbergen, H. W. Structural and magnetic properties of  $NiC_x$  and  $NiN_x$  (x = 0 to (1)/(3)) solid solutions from first-principles calculation. *Phys. Rev. B* **2012**, *86*, 134114.
- (47) Zhang, Y.; Zhu, Y.; Cao, Y.; Li, D.; Zhang, Z.; Wang, K.; Ding, F.; Wang, X.; Meng, D.; Fan, L.; Wu, J. Size and morphology-controlled synthesis of Ni<sub>3</sub>C nanoparticles in a TEG solution and their magnetic properties. *RSC Adv.* **2016**, *6*, 81989–81994.
- (48) Chen, C.; He, L.; Leng, Y.; Li, X. Weak ferromagnetism and spin-glass state with nanosized nickel carbide. *J. Appl. Phys.* **2009**, *105*, 123923.
- (49) Matsuda, J.; Yamamoto, T.; Takahashi, S.; Nakanishi, H.; Sasaki, K.; Matsumura, S. In Situ TEM Investigation of Structural Changes in Ni Nanoparticle Catalysts under Gas Atmospheres: Implications for Catalyst Degradation. *ACS Appl. Nano Mater.* **2021**, *4*, 2175–2182.
- (50) Xing, M.; Mohapatra, J.; Zeng, F.; Ping Liu, J. Magnetic properties of nickel carbide nanoparticles with enhanced coercivity. *AIP Adv.* **2018**, *8*, 056308.
- (51) Mourdikoudis, S.; Liz-Marzán, L. M. Oleylamine in Nanoparticle Synthesis. *Chem. Mater.* **2013**, 25, 1465–1476.
- (52) Jin, Z.; Wang, H.; Ma, Q. High Electron Conductivity of Ni/Ni<sub>3</sub>C Nanoparticles Anchored on C-Rich Graphitic Carbon Nitride for Obviously Improving Hydrogen Generation. *Ind. Eng. Chem. Res.* **2020**, *59* (19), 8974–8983.
- (53) Kim, S.-W.; Ro, J. C.; Suh, S.-J. Simple Synthesis and Characterization of Shell-Thickness-Controlled Ni/Ni<sub>3</sub>C Core-Shell Nanoparticles. *Nanomaterials* **2022**, *12* (12), 1954.
- (54) Zarenezhad, E.; Abdulabbas, H. T.; Marzi, M.; Ghazy, E.; Ekrahi, M.; Pezeshki, B.; Ghasemian, A.; Moawad, A. A. Nickel Nanoparticles: Applications and Antimicrobial Role against Methicillin-Resistant *Staphylococcus aureus* Infections. *Antibiotics* **2022**, *11*, 1208.
- (55) Jaji, N.-D.; Lee, H. L.; Hussin, M. H.; Akil, H. M.; Zakaria, M. R.; Othman, M. B. H. Advanced nickel nanoparticles technology: From synthesis to applications. *Nanotechnol. Rev.* **2020**, *9*, 1456–1480.
- (56) Javed, R.; Zia, M.; Naz, S.; Aisida, S. O.; Ain, N. u.; Ao, Q. Role of capping agents in the application of nanoparticles in biomedicine and environmental remediation: recent trends and future prospects. *J. Nanobiotechnol.* **2020**, *18*, 172.

- (57) Nemala, H.; Thakur, J. S.; Naik, V. M.; Vaishnava, P. P.; Lawes, G.; Naik, R. Investigation of magnetic properties of Fe<sub>3</sub>O<sub>4</sub> nanoparticles using temperature dependent magnetic hyperthermia in ferrofluids. *J. Appl. Phys.* **2014**, *116*, 034309.
- (58) Destyorini, F.; Irmawati, Y.; Hardiansyah, A.; Widodo, H.; Yahya, I. N. D.; Indayaningsih, N.; Yudianti, R.; Hsu, Y. I.; Uyama, H. Formation of Nanostructured Graphitic Carbon from Coconut Waste via Low-Temperature Catalytic Graphitisation. *Eng. Sci. Technol.* **2021**, 24 (2), 514–523.
- (59) Bayer, B. C.; Bosworth, D. A.; Michaelis, F. B.; Blume, R.; Habler, G.; Abart, R.; Weatherup, R. S.; Kidambi, P. R.; Baumberg, J. J.; Knop-Gericke, A.; Schloegl, R.; Baehtz, C.; Barber, Z. H.; Meyer, J. C.; Hofmann, S. In Situ Observations of Phase Transitions in Metastable Nickel (Carbide)/Carbon Nanocomposites. *J. Phys. Chem. C* 2016, 120 (39), 22571–22584.
- (60) Gan, P. P.; Ng, S. H.; Huang, Y.; Li, S. F. Y. Green synthesis of gold nanoparticles using palm oil mill effluent (POME): A low-cost and eco-friendly viable approach. *Bioresour. Technol.* **2012**, *113*, 132–135.
- (61) Ferreira, C. D.; da Conceição, E. J. L.; Machado, B. A. S.; Hermes, V. S.; de Oliveira Rios, A.; Druzian, J. I.; Nunes, I. L. Physicochemical Characterization and Oxidative Stability of Microencapsulated Crude Palm Oil by Spray Drying. *Food Bioprocess Technol.* **2016**, *9*, 124–136.
- (62) Ngnintedem Yonti, C.; Kenfack Tsobnang, P.; Lontio Fomekong, R.; Devred, F.; Mignolet, E.; Larondelle, Y.; Hermans, S.; Delcorte, A.; Lambi Ngolui, J. Green Synthesis of Iron-Doped Cobalt Oxide Nanoparticles from Palm Kernel Oil via Co-Precipitation and Structural Characterization. *Nanomaterials* **2021**, *11* (11), 2833.
- (63) Campos, A. C.; Paes, S. C.; Correa, B. S.; Cabrera-Pasca, G. A.; Costa, M. S.; Costa, C. S.; Otubo, L.; Carbonari, A. W. Growth of Long ZnO Nanowires with High Density on the ZnO Surface for Gas Sensors. ACS Appl. Nano Mater. 2020, 3, 175–185.
- (64) Carbonari, A. W.; Mestnik-Filho, J.; Saxena, R. N. Impurities in Magnetic Materials Studied by PAC Spectroscopy. *Defect Diffusion Forum* **2011**, *311*, 39–61.
- (65) Ul-Hamid, A.; Quddus, A.; Saricimen, H.; Dafalla, H. Corrosion Behavior of Coarse- and Fine-Grain Ni Coatings Incorporating NaH<sub>2</sub>PO<sub>4</sub>.H<sub>2</sub>O Inhibitor Treated Substrates. *Mater. Res.* 2015, 18, 20–26.
- (66) Costa, W. A.; Bezerra, F. W. F.; de Oliveira, M. S.; Andrade, E. H. d. A.; Santos, A. P. M. d.; Cunha, V. M. B.; Santos, D. C. S. d.; Banna, D. A. D. d. S.; Teixeira, E.; de Carvalho Junior, R. N. Supercritical CO<sub>2</sub> extraction and transesterification of the residual oil from industrial palm kernel cake with supercritical methanol. *J. Supercrit. Fluids* **2019**, *147*, 179–187.
- (67) Thanh, N. T. K.; Maclean, N.; Mahiddine, S. Mechanisms of Nucleation and Growth of Nanoparticles in Solution. *Chem. Rev.* **2014**, *114*, 7610–7630.
- (68) Klinger, M. More features, more tools, more *CrysTBox. J. Appl. Crystallogr.* **2017**, *50*, 1226–1234.
- (69) Xu, Y.; Tu, W.; Zhang, B.; Yin, S.; Huang, Y.; Kraft, M.; Xu, R. Nickel Nanoparticles Encapsulated in Few-Layer Nitrogen-Doped Graphene Derived from Metal-Organic Frameworks as Efficient Bifunctional Electrocatalysts for Overall Water Splitting. *Adv. Mater.* 2017, 29 (11), 1605957.
- (70) Shirley, D. A.; Rosenblum, S. S.; Matthias, E. Hyperfine fields at solutes in ferromagnets: cadmium and ruthenium in nickel. *Phys. Rev.* **1968**, *170*, 363–378.
- (71) Lindgren, B.; Karlsson, E.; Jonsson, B. Magnitude and direction of hyperfine fields for a Cd impurity in Ni at low and high magnetizing fields. *Hyperfine Interact.* **1975**, *1* (1), 505–516.
- (72) Zeitz, W.-D.; Dogra, R.; Byrne, A. P.; Shrestha, S. K.; Edge, A. V. J.; Timmers, H. Magnetism of isolated cadmium atoms in vacancy-associated sites in nickel. *Phys. Rev. B* **2008**, *78*, 014406.
- (73) Kowalik, P.; Bujak, P.; Penkala, M.; Maroń, A. M.; Ostrowski, A.; Kmita, A.; Gajewska, M.; Lisowski, W.; Sobczak, J. W.; Pron, A. Indium(II) Chloride as a Precursor in the Synthesis of Ternary (Ag—

- In-S) and Quaternary (Ag-In-Zn-S) Nanocrystals. *Chem. Mater.* **2022**, 34, 809-825.
- (74) Mahato, S. K.; Acharya, C.; Wellington, K. W.; Bhattacharjee, P.; Jaisankar, P. InCl<sub>3</sub>: A Versatile Catalyst for Synthesizing a Broad Spectrum of Heterocycles. *ACS Omega* **2020**, *5* (6), 2503–2519.
- (75) Neuhaus, P.; Herzig, C.; Gust, W. Grain Boundary Diffusion of Indium in Nickel and Nickel-Indium. *Acta Metall.* **1989**, 37 (2), 587–595.
- (76) Bai, Y.; Kirvassilis, D.; Xu, L.; Mavrikakis, M. Atomic and Molecular Adsorption on Ni(111). Surf. Sci. 2019, 679, 240–253.
- (77) Ferreira, W. L.; Pereira, L. F. D.; Leite Neto, O. F. S.; Maciel, L. S.; Gonçalves, V. C.; Saxena, R. N.; Carbonari, A. W.; Costa, M. S.; Cabrera-Pasca, G. A. Locally Symmetric Oxygen Vacancy around Cd Impurities in CeO<sub>2</sub>. *Phys. Rev. B* **2021**, *104* (3), 035146.
- (78) Blaha, P.; Schwarz, K.; Madsen, G.; Kvasnicka, D.; Luitz, J. WEN2K: An Augmented Plane Wave Plus Local Orbitals Program for Calculating Crystal Properties; Technische Universität Wien: Austria, 2001.
- (79) Dong, S. R.; el-Kateb, S.; Hooley, J. G.; Martin, P. W. Graphite indium chloride studied by time-differential perturbed angular correlations of  $\gamma$ -rays. *Solid State Commun.* **1983**, 45, 791–793.
- (80) Santos, R. V.; Cabrera-Pasca, G. A.; Costa, C. S.; Bosch-Santos, B.; Otubo, L.; Pereira, L. F. D.; Correa, B. S.; Effenberger, F. B.; Burimova, A.; Freitas, R. S.; Carbonari, A. W. Crystalline and magnetic properties of CoO nanoparticles locally investigated by using radioactive indium tracer. *Sci. Rep.* **2021**, *11*, 21028.
- (81) Rinneberg, H. H. Application of perturbed angular correlation to chemistry and related areas of solid state physics. *At. Energy Rev.* 1979, 17, 477–595.
- (82) Errico, L.; Lejaeghere, K.; Runco, J.; Mishra, S. N.; Renteria, M.; Cottenier, S. Precision of Electric-Field Gradient Predictions by Density Functional Theory and Implications for the Nuclear Quadrupole Moment and Its Error Bar of the <sup>111</sup>Cd 245 keV 5/2<sup>+</sup> Level<sup>111</sup>Cd 245 keV 5/2<sup>+</sup> Level. *J. Phys. Chem. C* **2016**, *120*, 23111–23120.
- (83) Haas, H.; Correia, J. G. The quadrupole moments of Zn and Cd isotopes—an update. *Hyperfine Interact.* **2010**, 198, 133–137.
- (84) Ramirez, F. E. N.; Cabrera-Pasca, G. A.; Mestnik-Filho, J.; Carbonari, A. W.; Souza, J. A. Magnetic and transport properties assisted by local distortions in Bi<sub>2</sub>Mn<sub>4</sub>O<sub>10</sub> and Bi<sub>2</sub>Fe<sub>4</sub>O<sub>9</sub> multiferroic compounds. *J. Alloys Compd.* **2015**, *651*, 405–413.
- (85) Schatz, G.; Weidinger, A. Nuclear Condensed Matter Physics: Nuclear Methods and Applications, 2nd ed.; J. Wiley and Sons: Chichester, United Kingdom, 1996; pp 63–99.
- (86) Schell, J.; Lupascu, D. C.; Carbonari, A. W.; Domingues Mansano, R.; Souza Ribeiro Junior, I.; Dang, T. T.; Anusca, I.; Trivedi, H.; Johnston, K.; Vianden, R. Ion implantation in titanium dioxide thin films studied by perturbed angular correlations. *J. Appl. Phys.* **2017**, *121*, 145302.
- (87) Darriba, G. N.; Muñoz, E. L.; Carbonari, A. W.; Renteria, M. Experimental TDPAC and Theoretical DFT Study of Structural, Electronic, and Hyperfine Properties in ( $^{111}\text{In} \rightarrow$ ) $^{111}\text{Cd-Doped SnO}_2$  Semiconductor: *Ab Initio* Modeling of the Electron-Capture-Decay After-Effects Phenomenon. *J. Phys. Chem. C* **2018**, *122*, 17423–17436.
- (88) Cabrera-Pasca, G. A.; Carbonari, A. W.; Bosch-Santos, B.; Mestnik-Filho, J.; Saxena, R. N. The effect of hybridization on local magnetic interactions at highly diluted Ce ions in tetragonal intermetallic compounds RERh<sub>2</sub>Si<sub>2</sub> (RE Ce, Pr, Nd, Gd, Tb, Dy). *J. Phys.: Condens. Matter* **2012**, 24, 416002.
- (89) Correa, E. L.; Bosch-Santos, B.; Freitas, R. S.; da Penha A Potiens, M.; Saiki, M.; Carbonari, A. W. Synthesis and atomic scale characterization of Er<sub>2</sub>O<sub>3</sub> nanoparticles: enhancement of magnetic properties and changes in the local structure. *Nanotechnology* **2018**, 29, 205704.
- (90) Bosch-Santos, B.; Carbonari, A. W.; Cabrera-Pasca, G. A.; Costa, M. S.; Saxena, R. N. Effect of Ge substitution for Si on the magnetic hyperfine field in LaMn<sub>2</sub>Si<sub>2</sub> compound measured by

- perturbed angular correlation spectroscopy with  $^{140}\mathrm{Ce}$  as probe nuclei. *J. Appl. Phys.* **2013**, *113*, 17E124.
- (91) Carbonari, A. W.; Saxena, R. N.; Mestnik-Filho, J.; Cabrera-Pasca, G. A.; Rao, M. N.; Oliveira, J. R. B.; Rizzuto, M. A. Study of the effect of disorder on the local magnetism in Heusler alloys. *J. Appl. Phys.* **2006**, *99*, 08J104.
- (92) Dogra, R.; Junqueira, A. C.; Saxena, R. N.; Carbonari, A. W.; Mestnik-Filho, J.; Moralles, M. Hyperfine interaction measurements in LaCrO<sub>3</sub> and LaFeO<sub>3</sub> perovskites using perturbed angular correlation spectroscopy. *Phys. Rev. B* **2001**, *63*, 224104.